mathematics

Article

Numerical Simulation of Failure Modes in Irregular Columnar Jointed Rock Masses under Dynamic Loading

Yingjie Xia [1,2,3], Bingchen Liu [2,3], Tianjiao Li [2,3,*], Danchen Zhao [2,3], Ning Liu [4], Chun'an Tang [2,3] and Jun Chen [4]

[1] State Key Laboratory of Geomechanics and Geotechnical Engineering, Institute of Rock and Soil Mechanics, Chinese Academy of Sciences, Wuhan 430071, China; xiayingjie@dlut.edu.cn
[2] State Key Laboratory of Coastal and Offshore Engineering, Dalian University of Technology, Dalian 116024, China
[3] School of Civil Engineering, Dalian University of Technology, Dalian 116024, China
[4] Power China Huadong Engineering Corporation, Hangzhou 310014, China
* Correspondence: tianjiaoli@dlut.edu.cn; Tel.: +86-158-4062-1813

Abstract: The mechanical properties and failure characteristics of columnar jointed rock mass (CJRM) are significantly influenced by its irregular structure. Current research on CJRMs is mainly under static loading, which cannot meet the actual needs of engineering. This paper adopts the finite element method (FEM) to carry out numerical simulation tests on irregular CJRMs with different dip angles under different dynamic stress wave loadings. The dynamic failure modes of irregular CJRMs and the influence law of related stress wave parameters are obtained. The results show that when the column dip angle α is 0°, the tensile-compressive-shear failure occurs in the CJRMs; when α is 30°, the CJRMs undergo tensile failure and a small amount of compressive shear failure, and an obvious crack-free area appears in the middle of the rock mass; when α is 60°, tensile failure is dominant and compressive shear failure is minimal and no crack area disappears; and when α is 90°, the rock mass undergoes complete tensile failure. In addition, in terms of the change law of stress wave parameters, the increase in peak amplitude will increase the number of cracks, promote the development of cracks, and increase the proportion of compression-shear failure units for low-angle rock mass. The changes in the loading and decay rate only affect the degree of crack development in the CJRMs, but do not increase the number of cracks. Meanwhile, the simulation results show that the crack expansion velocity of the CJRMs increases with the increase in dip angle, and the CJRMs with dip angle α = 60° are the most vulnerable to failure. The influence of the loading and decay rate on the rock mass failure is different with the change in dip angle. The results of the study provide references for related rock engineering.

Keywords: columnar jointed rock mass; numerical simulation; rock failure process analysis; dynamic loading; rock damage

MSC: 74S05

Citation: Xia, Y.; Liu, B.; Li, T.; Zhao, D.; Liu, N.; Tang, C.; Chen, J. Numerical Simulation of Failure Modes in Irregular Columnar Jointed Rock Masses under Dynamic Loading. *Mathematics* **2023**, *11*, 3790. https://doi.org/10.3390/math11173790

Academic Editors: Xin Cai, Shaofeng Wang and Xueming Du

Received: 5 August 2023
Revised: 28 August 2023
Accepted: 31 August 2023
Published: 4 September 2023

1. Introduction

As a unique geological structure of basalt, the columnar joint is a primary tensile fracture structure [1–4]. Many scholars believe that it is formed by cooling condensation and contraction of unexposed magma after volcanic eruption [5–7]. Due to the difference in magma cooling time, the cross-section of CJRMs shows a variety of irregular polygons, such as quadrilaterals, pentagons, and hexagons [8,9]. Meanwhile, compared with other rock masses because of the unique structure and formation mode, CJRMs exhibit complex discontinuity, non-uniformity, and strong anisotropy [10], which bring difficulties and challenges to some large-scale geotechnical hydropower, mining tunnel basting excavation projects [11].

With the construction of large hydropower stations, such as Tongjiezi, Xiluodu, and Baihetan, a large area of CJRMs were exposed and revealed as engineering rock masses, as in Figure 1, and related geotechnical engineering problems have followed, among which the stability of hydropower stations during blasting excavation is a great challenge [12–15]. The research methods of CJRMs mainly include mechanical tests, theoretical analysis, and numerical simulation [16–20]. Field tests and prototype observation are important means to study the mechanical properties of rock mass and are also the main basis for theoretical analysis. Jiang et al. [21] and Xia et al. [22] elucidated the anisotropy of columnar jointed basalts by in situ P-wave test. Fan et al. [23] and Shi et al. [24] have comprehensively clarified the mechanical properties, deformation characteristics, and failure modes of columnar jointed basalts under different boundary conditions via in situ tests and field monitoring. Laboratory tests are generally divided into rock tests and model tests, which overcome problems of high cost, low efficiency, and high data discreteness in field tests [25–28]. Jiang et al. [29–31] explained the influence of cracks on rock mass failure mode and joint concavity on anisotropy via laboratory tests. Based on theoretical analysis, Sonmez et al. [18] proposed a new method for the anisotropy classification of jointed rock mass. In addition, natural columnar joints have different joint dip angles. Jin et al. [11] and Xiao et al. [32] analyzed the relationship between joint dip angles and rock mass strength and deformation modulus via laboratory tests. At the same time, with the development of rock mechanics, numerical simulation is widely used in all aspects of rock mechanics properties [33]. Liu et al. [19] systematically elaborated on the size-dependence of jointed basalts and discussed the different failure modes of basalts at different scales.

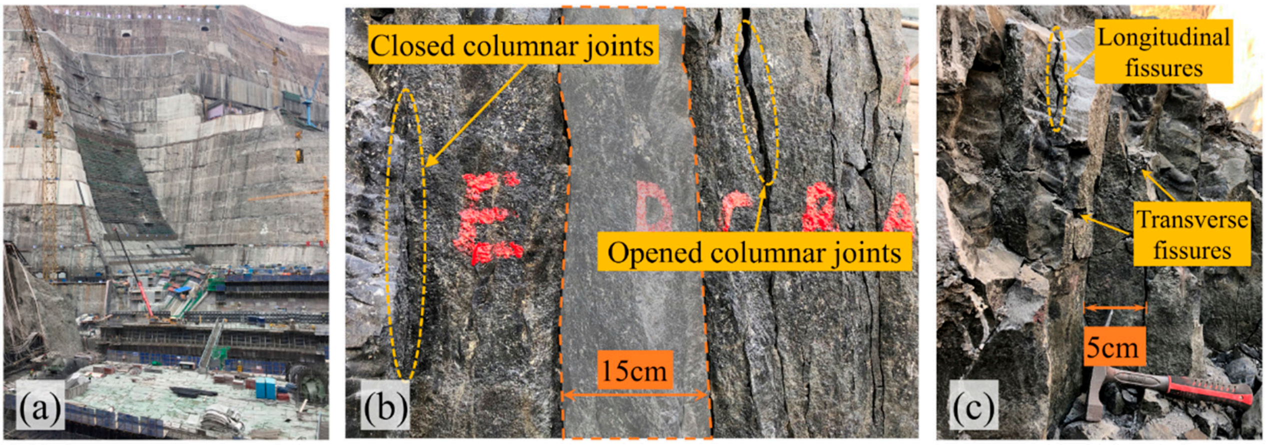

Figure 1. Structural characteristics of CJRMs: (**a**) left bank of Baihetan hydropower station; (**b**) columnar joints; (**c**) fissures.

However, the above studies on CJRMs considered the rock masses under static load, while the rock masses are often subjected to impact loads such as earthquakes and blasting in engineering [34], leading to catastrophic damage. Therefore, one of the practical problems in engineering is to study the mechanical behavior of rock under dynamic loadings. In the laboratory, the Split Hopkinson Pressure Bar system (SHPB) is usually used for dynamic loading analysis of rock samples to analyze the dynamic hazards of rock in engineering [35–38]. Chang et al. [39] analyzed the effect of loading rate on the dynamic fracture behavior of laminated micrite. Pei et al. [40] analyzed the dynamic tensile response of sandstone under different loading rates. Li et al. [41] pointed out that dynamic loading produces tensile failure under low-axial static pressure. Gong et al. [42] systematically studied the influence of strain rate on the dynamic strength of sandstone. Moreover, for jointed rocks, the interaction between stress waves and joints and cracks becomes the focus of rock dynamics research [43,44]. Huang et al. [45] learned by impact loading tests that the energy propagation coefficient decreases with the increase in joint inclination angle. Wang et al. [46] pointed out that the rock dynamic stress–strain curve can be divided into four stages: elastic, plastic, crack unsteady propagation, and post-failure, and proposed the damage weight theory of joint position. Li et al. [47] systematically studied the transmission and reflection law of stress waves traversing a single fractal joint. Meanwhile, numerical simulations are also widely used to study the dynamic mechanical properties of rocks. Wang et al. [48] studied the dynamic fracture propagation process of jointed rock masses under explosion loading by LS-DYNA and UEDC. Zhang et al. [49] modified the dynamic tensile model by using the improved DDA method. RFPA is also used to study the dynamic mechanical behavior of rocks [50]. Islam and Shaw [51] simulated crack initiation and propagation under dynamic load and proposed a new numerical method in good agreement with experimental results. And Yilmaz et al. [52] used FLAC3D to study the mechanical behavior of two different rock masses under blasting loads and applied the Mohr–Coulomb criterion to evaluate the damage of rock mass. Qian et al. [53] performed dynamic simulations on fractured rock mass with different angles and pointed out that crack dip angle has a huge influence on the fracture expansion and failure mode of rock masses. At the same time, jointed rock shows different mechanical properties and failure modes under different dip angles, so it is very important to explore the influence of dip angle on jointed rock. In addition, the dynamic constitutive models of jointed rock were studied extensively. Liu et al. [54] proposed a dynamic damage constitutive model, coupling the macroscopic and mesoscopic flaws, and pointed out that the peak strength of rock masses gradually decreases and tends to be stable when the number of joints increases. At the same time, based on the influence of joints on stress waves and the dynamic characteristics of the jointed rock mass, the dynamic damage model [55] and equivalent continuous medium model [56,57] of jointed rock mass are also proposed.

Moreover, stress wave parameters are rarely involved in the research of rock mechanical behavior and failure mode under dynamic conditions. Some scholars have analyzed the effect of a single parameter on rock mechanical behavior using relevant experiments, such as the influence of loading rate on the dynamic fracture behavior of rocks [58,59] and the influence of loading rate and peak amplitude on the dynamic evolution of fractures [60]. However, the studies did not take into account the interaction of multiple parameters, lacking a comprehensive analysis of waveform parameters on the dynamic mechanical properties of rock masses.

In this paper, CT scanning, Weibull distribution [61], and the finite element method (FEM) are used to establish numerical models of columnar jointed rock mass based on 3D printed samples of irregular columnar jointed rock mass with different angles established by Xia et al. [62]. By conducting numerical simulation under different dynamic loading conditions, the effects of peak value, loading rate, decay rate, and column dip angle on dynamic mechanical characteristics and failure mode of CJRMs are analyzed. Subsequently, the influences of dip angle and dynamic loading conditions on the mechanical properties of CJRMs are summarized. The results of this study can provide references for the dynamic stability analysis of CJRM engineering and the design and construction of geotechnical projects.

2. Methods

The dynamic mechanical behavior of CJRMs is a three-dimensional problem with a complex rock matrix and involves a failure process and crack development. Therefore, the dynamic numerical simulation of rock mass should meet the following requirements: (1) it should accurately reflect the complex structure of rock mass; and (2) it should be able to simulate the entire dynamic failure process of rock mass. In this study, a finite element method (FEM) based simulator RFPA^{3D}-CT (V1.0) developed by Mechsoft Technology(Dalian), considering Weibull distribution and equivalent continuous damage mechanics, was used to simulate the damage evolution process of CJRMs under dynamic loading.

In the numerical model, elastic damage mechanics are used to describe the meso-mechanical properties of rock. Figure 2 shows the constitutive relationship of an element under uniaxial stress [63], where f_c and f_t indicate the uniaxial compressive and tensile strength of the element and f_{cr} and f_{tr} represent the residual strength of an element after phase transformation.

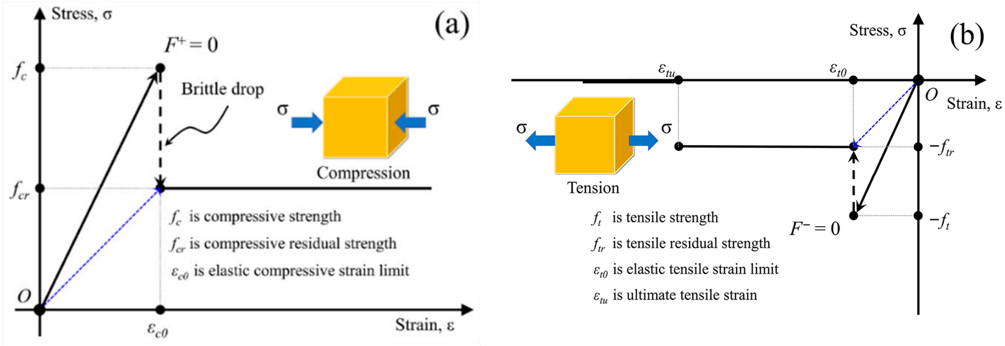

Figure 2. Constitutive relation of rock under uniaxial stress: (**a**) uniaxial compression; (**b**) uniaxial tension [63].

When the stress of the meso-element reaches the tensile strength, the element will have tensile damage, and the damage variable should meet the following requirements:

$$D = \begin{cases} 0, (\bar{\varepsilon} \geq \varepsilon_{t0}) \\ 1 - \frac{\lambda \varepsilon_{t0}}{\varepsilon}, (\varepsilon_{t0} \geq \bar{\varepsilon} \geq \varepsilon_{tu}) \\ 1, (\bar{\varepsilon} \leq \varepsilon_{tu}) \end{cases} \tag{1}$$

where λ is the residual strength coefficient of the element; and $\bar{\varepsilon}$, ε_{t0}, and ε_{tu} are the equivalent strain, elastic tensile strain, and ultimate tensile strain, respectively. When the tensile strain exceeds the ultimate tensile strain, the meso-element completely fails. In the three-dimensional state, the equivalent strain $\bar{\varepsilon}$ is usually used to replace the tensile strain ε:

$$\bar{\varepsilon} = -\sqrt{\langle -\varepsilon_1 \rangle^2 + \langle -\varepsilon_2 \rangle^2 + \langle -\varepsilon_3 \rangle^2} \tag{2}$$

Among them, ε_1, ε_2, ε_3 are the three principal strains of the element, and $\langle \ \rangle$ is operated as in Equation (3).

$$\langle x \rangle = \begin{cases} x, & x \geq 0 \\ 0, & x < 0 \end{cases} \tag{3}$$

When the stress value of the element meets the compression/shear criterion of Equation (4), the element can be considered to have compression/shear failure. In this case, the damage variable of the element can be expressed in accordance with Equation (5).

$$\frac{1 + \sin\varphi}{1 - \sin\varphi}\sigma_1 - \sigma_3 \geq \sigma_c \tag{4}$$

$$D = \begin{cases} 0, & \varepsilon < \varepsilon_c \\ 1 - \frac{\lambda \varepsilon_c}{\varepsilon}, & \varepsilon \geq \varepsilon_c \end{cases} \tag{5}$$

To realistically reflect the heterogeneity of rock materials, the mechanical properties of meso-elements, such as elastic modulus and strength, are assumed to meet Weibull distribution [61]:

$$\varphi(\alpha) = \frac{m}{\alpha_0} \cdot \left(\frac{a}{\alpha_0}\right)^{m-1} \cdot e^{-\left(\frac{a}{\alpha_0}\right)^m} \tag{6}$$

where α is the mechanical property parameter of rock element; α_0 is the mean value of physical properties; m is the homogeneity index; and $\varphi(\alpha)$ is the statistical distribution density of the mechanical properties, where the larger m is, the more uniform the material inside the rock is.

In the process of the dynamic finite element calculation, the space is discretized according to the Hamilton variational principle, and the dynamic equation is obtained as follows:

$$M\ddot{u} + C\dot{u} + Ku = Q \tag{7}$$

$\ddot{u}$, $\dot{u}$, and u represent acceleration, velocity, and displacement vectors, respectively; M, C, and K are the mass, damping, and stiffness matrices of the system, respectively. Q is the Force.

The numerical method was validated by many researchers [64–68].

3. Numerical Modeling and Parameter Calibration

In order to study the dynamic mechanical characteristics and failure modes of irregular CJRM samples under different dynamic loading conditions, four numerical models of rock mass with 0°, 30°, 60° and 90° in dip angle were established. According to the reconstruction of CJRMs and the establishment of numerical models [62,69,70], parameters of the numerical model are validated by the static loading experimental results first, and the dynamic mechanical characteristics and failure modes of the CJRM samples under different dynamic loading schemes are studied.

3.1. Establishment of the Numerical Simulation Model

According to the model-building method proposed by Xia et al. [71,72] and Zhao et al. [69], the digital models of irregular CJRMs with four different dip angles were established using a certain number of slices. The corresponding numerical models of CRJMs were built in numerical software, as shown in Figure 3a. The precision of meshing greatly affects the time of numerical calculation, the process of crack propagation, and the accuracy of the calculation. A numerical model of CJRM of 100 mm × 100 mm × 200 mm was established, and the mesh size is 1 mm, as shown in Figure 3c, to increase calculation efficiency and ensure the accuracy of the calculation. Considering that the stress loading area will change slightly when the boundary elements damage or fail. Therefore, in order to ensure uniform stress and long duration, high-strength ends are set on both sides of the numerical model, as shown in Figure 3b.

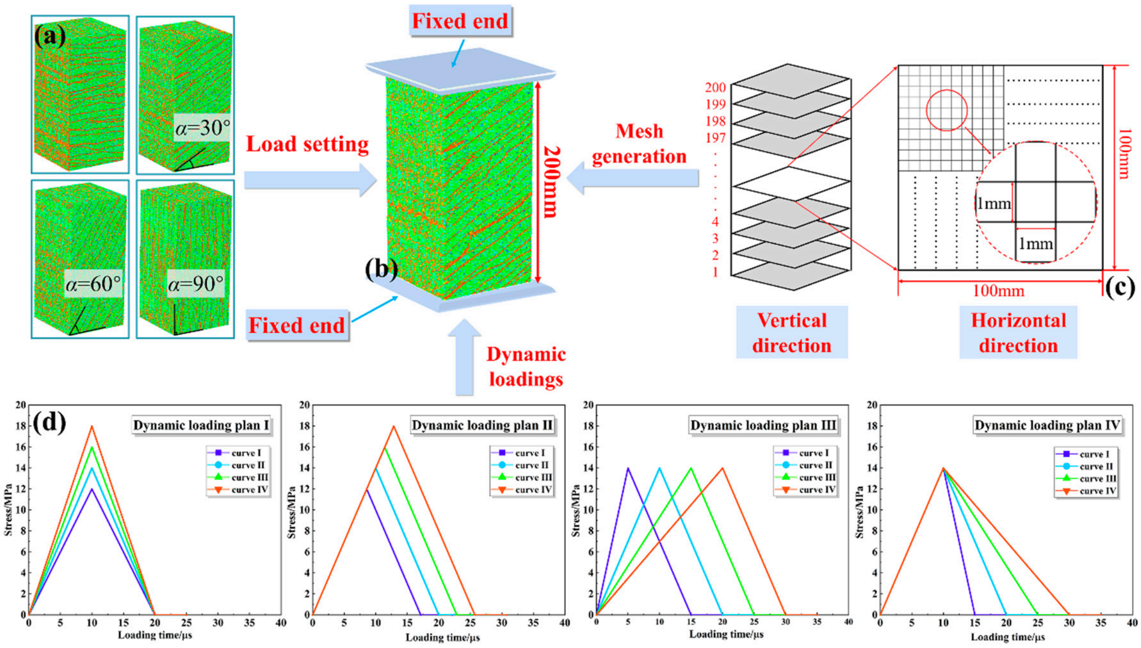

Figure 3. Numerical model under dynamic loading: (**a**) numerical model of the CJRMs; (**b**) load settings; (**c**) mesh generation; (**d**) loading plans.

3.2. Calibration of Numerical Model Parameters

The calibration of mechanical parameters is a prerequisite for accurate numerical simulation results. In this model, the parameters of rock and columnar joints are mainly calibrated. The rock mechanical parameters are obtained directly via physical tests, and those of the columnar joints are determined indirectly because of their complex structure. In parameter calibration, core drilling and freezing sampling of CJRM were carried out. The sample size should meet the requirements of the International Society for Rock Mechanics (ISRM) [73]. In the uniaxial compression test, the size of the sample is 50 mm in diameter and 100 mm in height, while in the shear test, it is 50 mm in height. CT scanning and laboratory physical tests were conducted on the CJRMs, as shown in Figure 4, to obtain the sample sections, stress–strain curves, and failure modes. The geometry of the numerical model was consistent with the physical sample. In the simulation, columnar joints are treated as elements with relatively weak elastic modulus and low strength, and their mechanical parameters are determined by the indirect method in reference [72]. The mechanical parameters of the rock matrix and joint were obtained by comparing the results of the numerical simulations and the laboratory tests with the trial-and-error method. The stress–strain curve and shear stress-displacement curves obtained from the simulations were compared with those obtained from the laboratory uniaxial compression test and shear tests. The parameters were adjusted continuously until the curves matched. The numerical mechanical parameters after calibration are shown in Table 1.

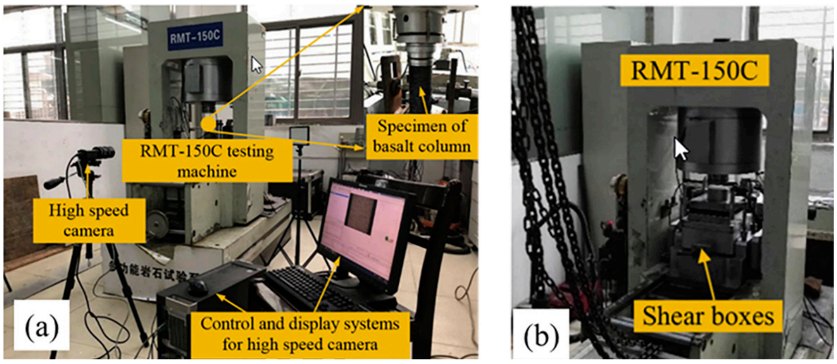

Figure 4. Physical laboratory experiments: (**a**) uniaxial compression test system; (**b**) columnar joint shear test [22].

Table 1. Mechanical parameters in numerical simulation.

Materials	Elastic Modulus/GPa	Compressive Strength/MPa	Poisson's Ratio	Density (g/cm^3)	Fraction Angle/°	C-T Ratio *
Rock	50	300	0.25	2.58	30	10
Joint	10	30	0.35	2.58	15	20
Fixed end	50	30,000	0.25	2.58	30	10

* C-T ratio is the ratio of compression strength to tensile strength.

3.3. Dynamic Loading Parameter Setting

Nowadays, the typical triangular distributed load model and exponential distributed load model are adopted in the analysis of explosion-induced stress waves. Because of the simple form of triangular load distribution and the accurate expression of the basic characteristics of an explosion, it is widely used in practical applications. In this paper, triangular stress waves are also used to simulate an explosion applied on CJRM. Meanwhile, in order to study the influence of stress wave parameters on mechanical properties and failure modes of the CJRM under dynamic loading, the CJRM is subjected to different peak amplitudes with different loading/decay rates (loading plan I), different peak amplitudes with the same loading/decay rate (loading plan II), different loading rates with the same decay rate (loading plan III), and different decay rates with the same loading rate (loading plan IV), for a total of 16 stress waves with different waveforms, as shown in Figure 3d. In loading plan I, the peak amplitude of 12 MPa, 14 MPa, 16 MPa, and 18 MPa was finally selected after preliminary trial calculation to prevent the rock mass from being damaged in advance due to excessive peak value. The loading rate to reach the peak amplitude is 5 μs, 10 μs, 15 μs, and 20 μs, and the influence of high and low rates on the failure mode of rock mass was studied, as well as the decay rate. The effects of stress waveform parameters (peak amplitude, loading rate, and decay rate) on the dynamic mechanical properties and failure modes of CJRMs are comprehensively compared. For the accuracy and efficiency of the calculation, the dynamic time step is set as 0.5 μs.

4. Numerical Simulation Results

4.1. Dynamic Failure Mode and Acoustic Emission Characteristics

Figure 5 shows the failure modes of numerical models with different dip angles α at the peak value of 12 MPa. In the Acoustic Emission (AE), blue dots are the tensile failure events, and red dots are the compression-shear failure events. Figure 6 shows the single-step AE energy curves of models with different dip angles α at the peak value of 12 MPa. The yellow, green and blue backgrounds in the figure mark foreshock, mainshock and aftershock, respectively.

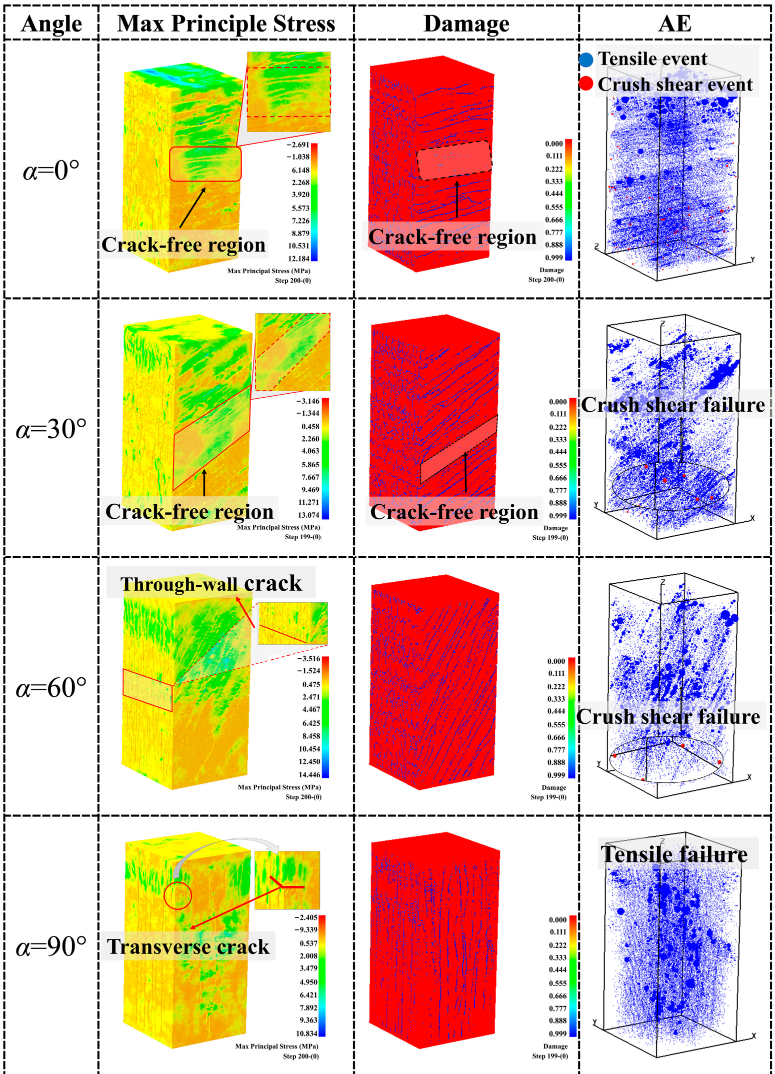

Figure 5. Numerical results of models with different column dip angles α at the peak amplitude of 12 MPa.

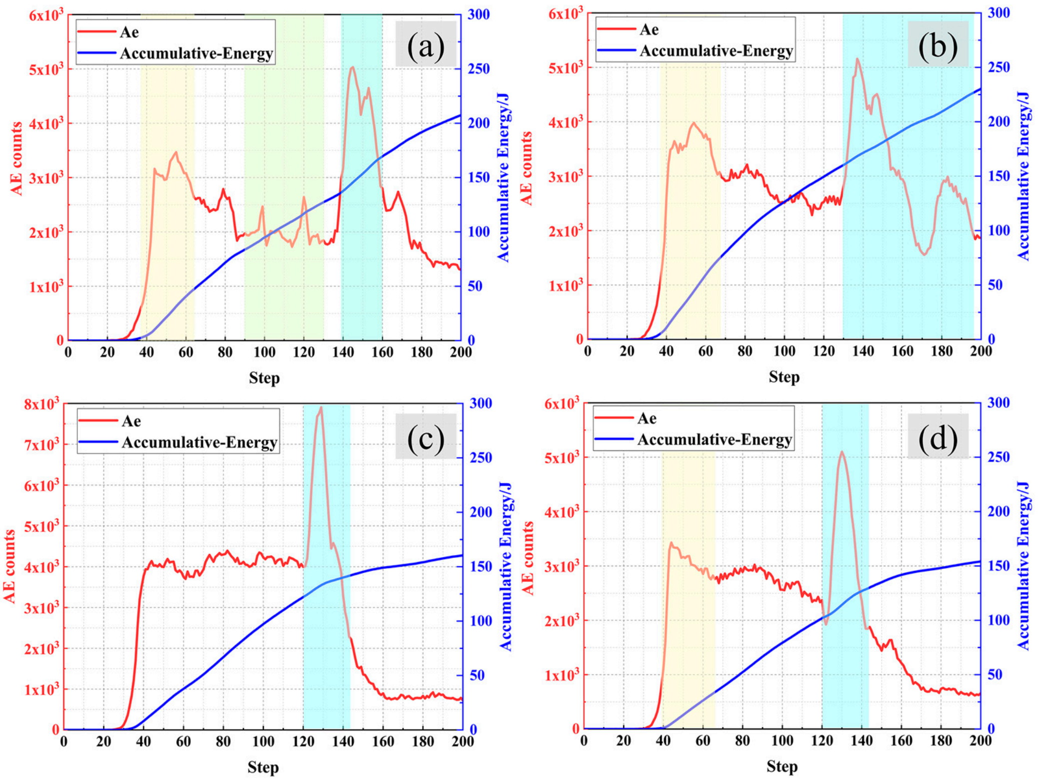

Figure 6. Single-step AE energy curves of models with different column dip angles α at the peak amplitude of 12 MPa: (**a**) α = 0°; (**b**) α = 30°; (**c**) α = 60°; (**d**) α = 90°.

For α = 0°, when the stress wave begins to transfer, the crack sprouts at the bottom and develops upward gradually with a certain lag phenomenon compared to the stress propagation. Then, the upper part generates cracks and gradually transmits downward. At the same time, the cracks at the lateral joints develop further along the joints, forming through-cracks. At this dip angle, the compression-shear cracks are first generated, and then the tensile cracks initiate and propagate. The failure elements are distributed parallel to the joint surface, and there is a tensile AE events aggregation area at the axial top. The AE energy is manifested as a multi-modal "foreshock—mainshock—aftershock" [74]. When α = 30°, the crack development mode is similar to 0°. The region without through-wall cracks in the middle of the model decreases, and the crack germination rate is faster. At this angle, the tensile cracks are produced first. In terms of failure type, tensile failures are distributed in the main position, except for a small number of compression-shear failures, which are distributed in the bottom and middle of the rock mass. The AE energy is a multi-model "foreshock—aftershock". At α = 60°, the cracks germinate in the lower left corner of the numerical model and gradually develop upward to the right along the joint surface. It extends to the top, and an obvious through-wall crack appears in the middle of the rock mass. Tensile failures occupy the entire model, and few compression-shear failures are distributed at the bottom of the rock mass. The AE energy shows a unimodal "aftershock". When α = 90°, the crack germination rate is consistent with the stress propagation rate. The cracks are generated from the bottom of the rock mass and expand along the joint surface, forming vertical tensile cracks along the joint direction. The failure mode of meso elements is all tensile failure. The stress on the top side column exceeds the tensile strength, resulting in an obvious transverse tensile crack. The AE energy appears as a bimodal "foreshock—aftershock".

Figure 7 is the picture of stress and crack evolution of the α = 30° model during a loading time of 20 μs and the peak stresses of 12 MPa, 14 MPa, 16 MPa, and 18 MPa, respectively. Vertically, the propagation velocity of vertical cracks under different peak stresses is much higher than that along the joint direction, and the joint direction cracks show a certain hysteresis phenomenon. Horizontally, the stress distribution in the initial loading stage is basically the same. The stress distribution under different peak stress varies in the late loading stage. When the peak stress is small, the number of failure cracks is small and mainly distributed at the top of the rock mass. With the increase in peak stress, the number of cracks increases, and they are distributed in the top, middle, and bottom of the rock mass. In addition, for the 200 steps, the crack development degree generally increases with the increase in peak stress. Therefore, the crack development is affected by the peak stress, loading rate, and decay rate.

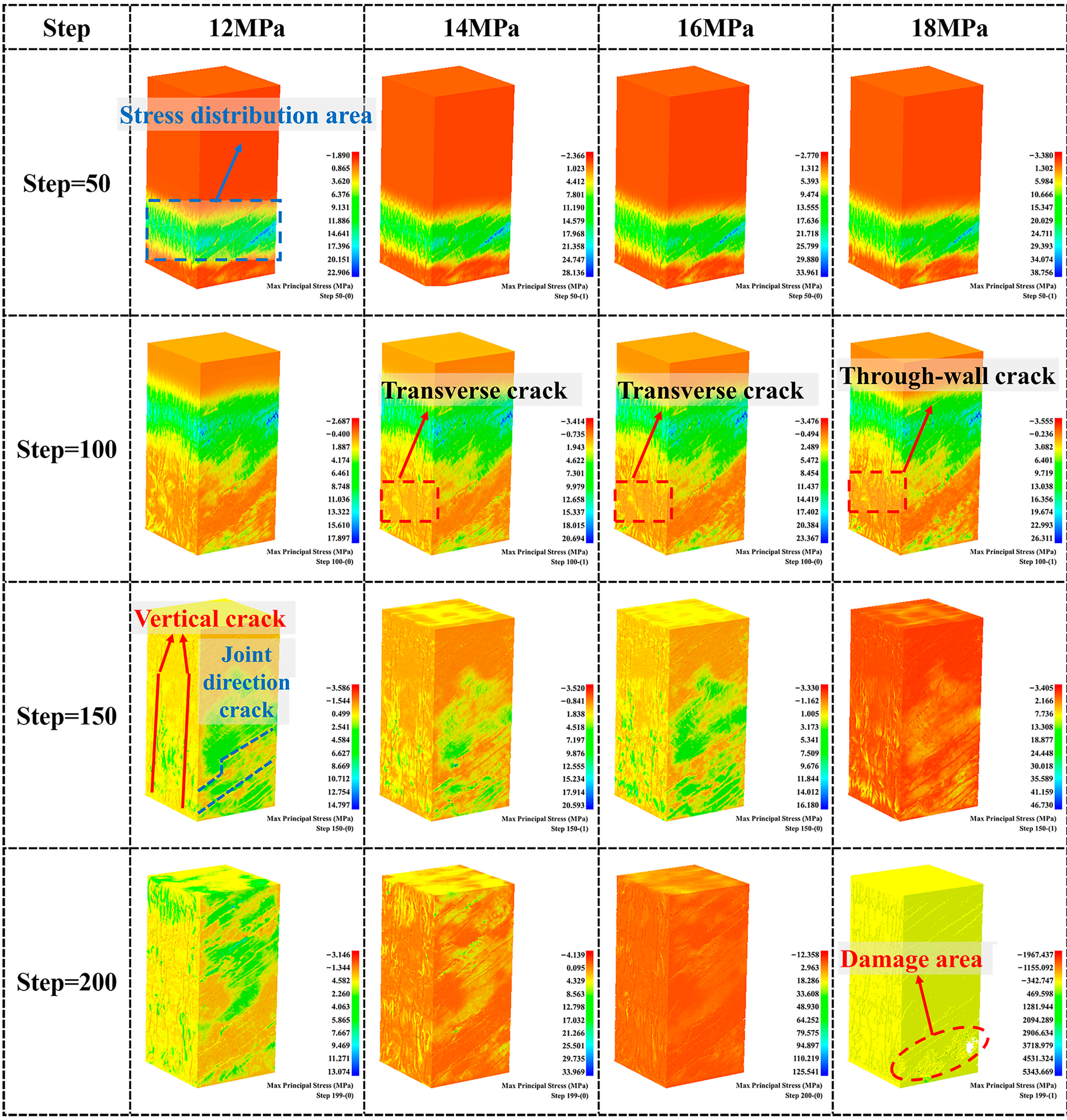

Figure 7. Numerical results of the CJRM with $\alpha = 30°$ under loading plan I.

The stress nephogram of CJRMs under the loading plan I is shown in Figure 8. When $\alpha = 0°$, the penetrating cracks are concentrated in the top and bottom of the rock mass, and the area without cracks is larger. The through-wall cracks are formed at the position of the joints. The maximum principal stress in rock mass increases with the increase in peak stress. When $\alpha = 60°$, the fractured volume increases first and then decreases with the increase in peak stress, and the failure moment of rock mass is advanced. The penetrating cracks mainly concentrate in the middle of the rock mass. There is no through-wall crack at the bottom and no obvious crack-free region. When $\alpha = 90°$, the cracks mainly occur at the vertical joints, and the transverse crack occurs at the top and gradually develops into a through-wall crack. The cracks are tensile cracks, and there is no obvious crack-free region on the surface of the rock mass.

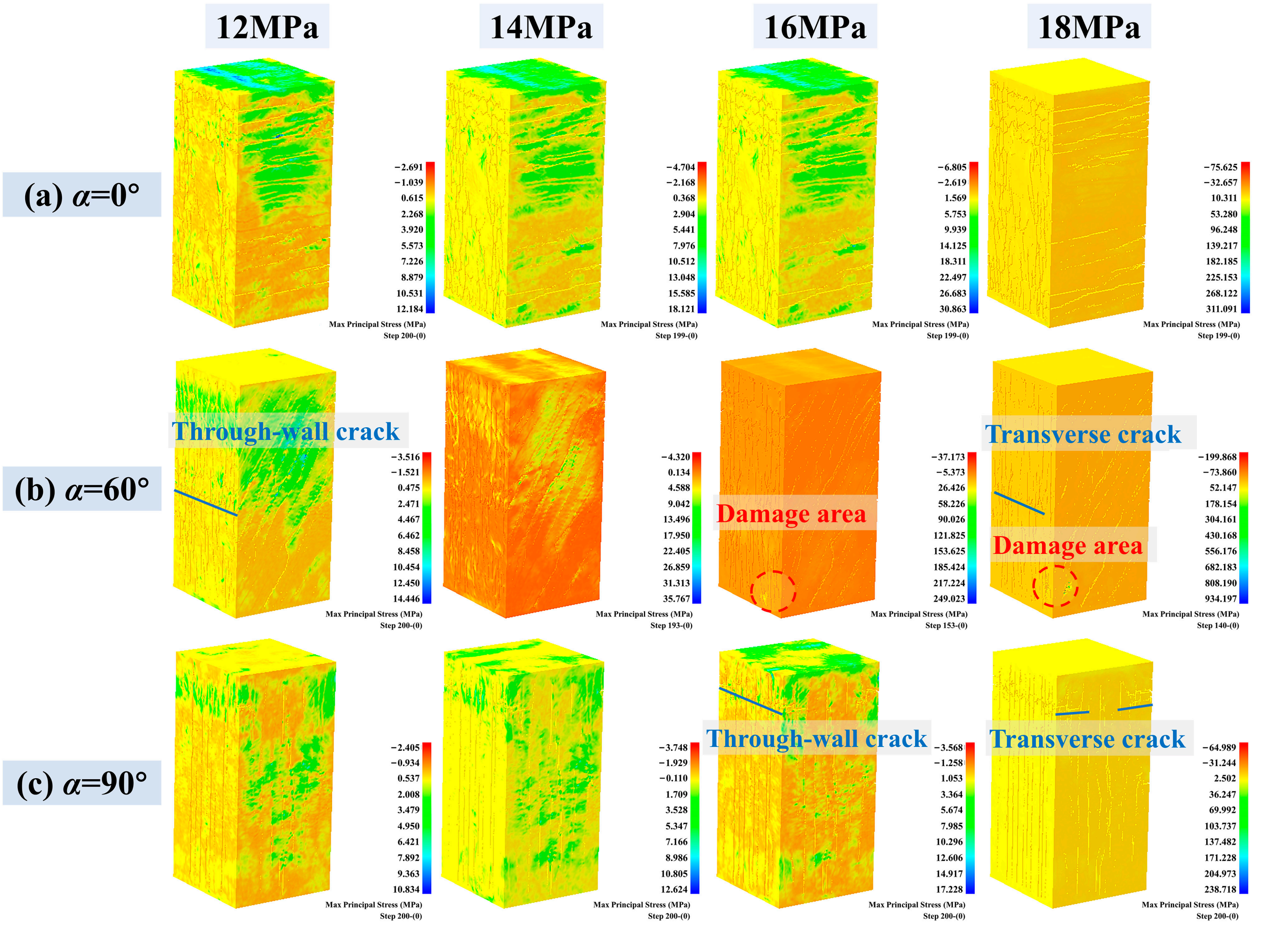

Figure 8. Stress nephogram of the CJRMs under the loading plan I: (**a**) $\alpha = 0°$; (**b**) $\alpha = 60°$; (**c**) $\alpha = 90°$.

Figure 9 shows the AE event image of the loading plan I. The AE events are concentrated at the top of the rock mass and parallel to the joints. In particular, some accumulation area of tensile failure of $\alpha = 90°$ rock mass is perpendicular to the vertical joint. With the increase in peak stress, the distribution range and density of compression-shear failure elements increase, and the proportion of compression-shear failure increases. The energy and distribution of tensile AE events are more uniform, and the failure time is earlier. The AE cloud image of $\alpha = 60°$ rock mass is the most obvious, and the tensile AE events release more energy in the early stage of loading. It is also seen from Figure 10a that the number of AE events increases linearly with the increase in peak stress. In addition, rock mass with $\alpha = 60°$ increases most significantly.

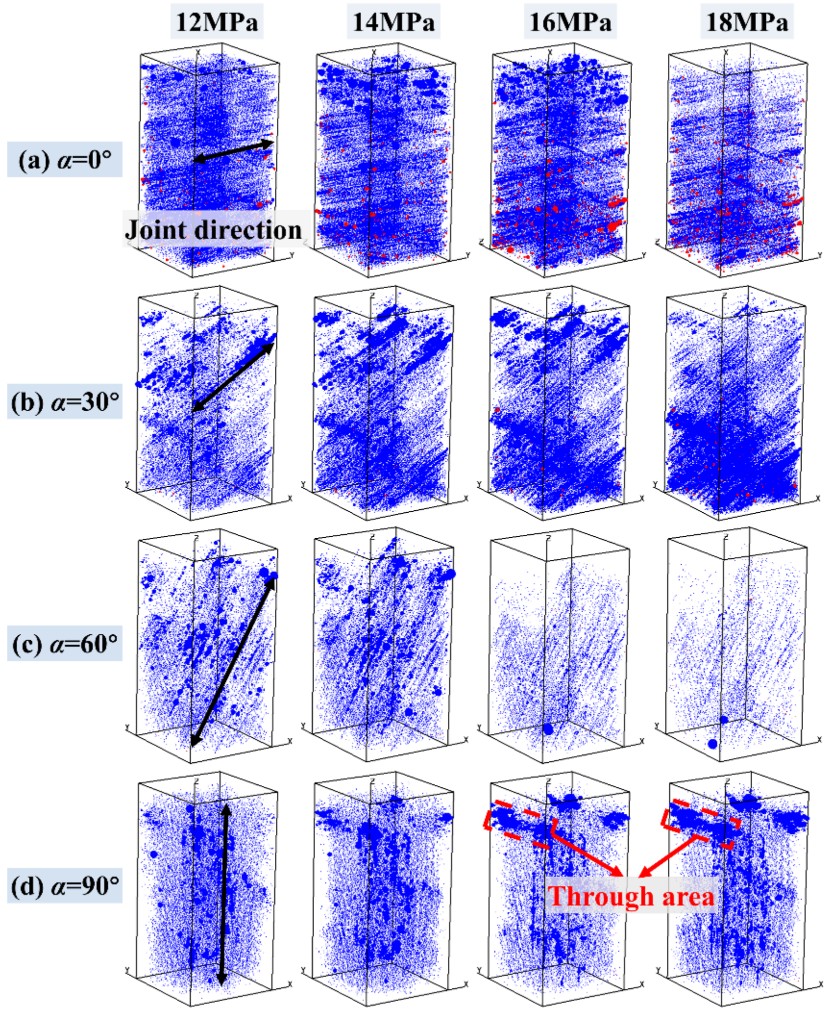

Figure 9. AE diagram of the CJRMs under the loading plan I: (**a**) α = 0°; (**b**) α = 30°; (**c**) α = 60°; (**d**) α = 90°.

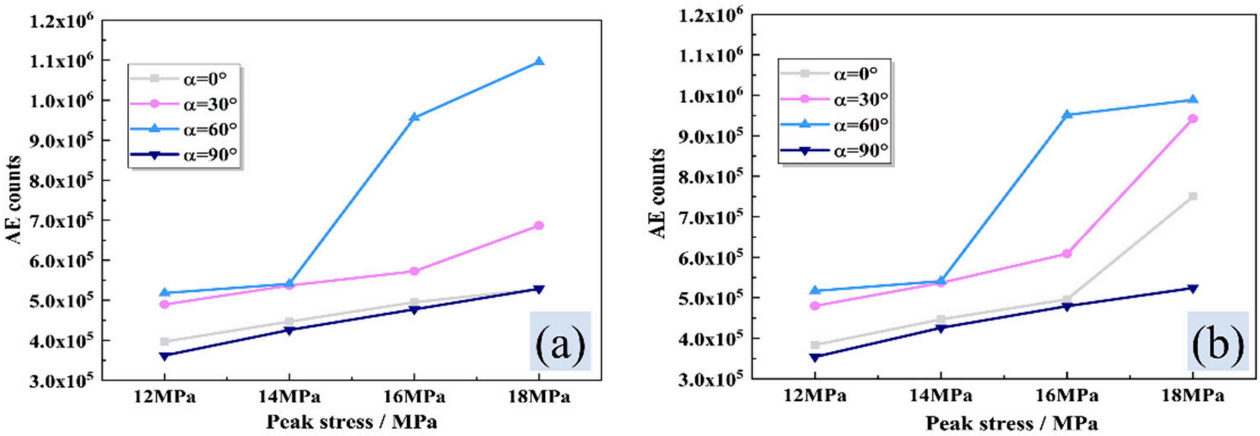

Figure 10. AE events under different peak amplitudes: (**a**) Loading plan I; (**b**) Load plan II.

4.2. Effect of Stress Peak on Failure Mode and AE of Rock Mass

Figure 11 shows the numerical simulation results of the CJRM numerical models under the condition that only the peak stress is changed. When the peak stress increases, the maximum principal stress inside the rock mass increases, and the failure time is advanced. When the peak stress is too large, the through-wall cracks cannot be formed. When α = 0°, the increase in peak stress within a certain range makes the through-wall cracks loading, mainly distributed at the top and bottom of the rock mass, and there is a crack-free area in the middle. When $\alpha = 30°$, the number of lateral through-wall cracks increases with the increase in the peak stress at low peak stress. However, when the peak stress is high, the failure time of rock mass is advanced, and the lateral cracks cannot be developed completely, so the number of cracks does not change or even decrease, such as 16 MPa. When $\alpha = 60°$, the cracks germinate from the bottom of the rock mass and extend upward continuously along the joints. The propagation of the crack is inhibited by the transverse penetrating crack, which is in the middle of the rock mass instead of the top. Meanwhile, the fractured volume is greatly increased. The crack propagation pattern of $\alpha = 90°$ rock mass is consistent with the joint direction and increases with the peak stress; the number of vertical cracks also increases, and the stress concentration area becomes smaller. The transverse crack appears at the top of the rock mass and extends to the interior of the rock mass, forming a transverse penetration crack, which is a tensile crack. In conclusion, the peak amplitude applied to rock mass can increase the number of cracks and promote the development of cracks within a certain range.

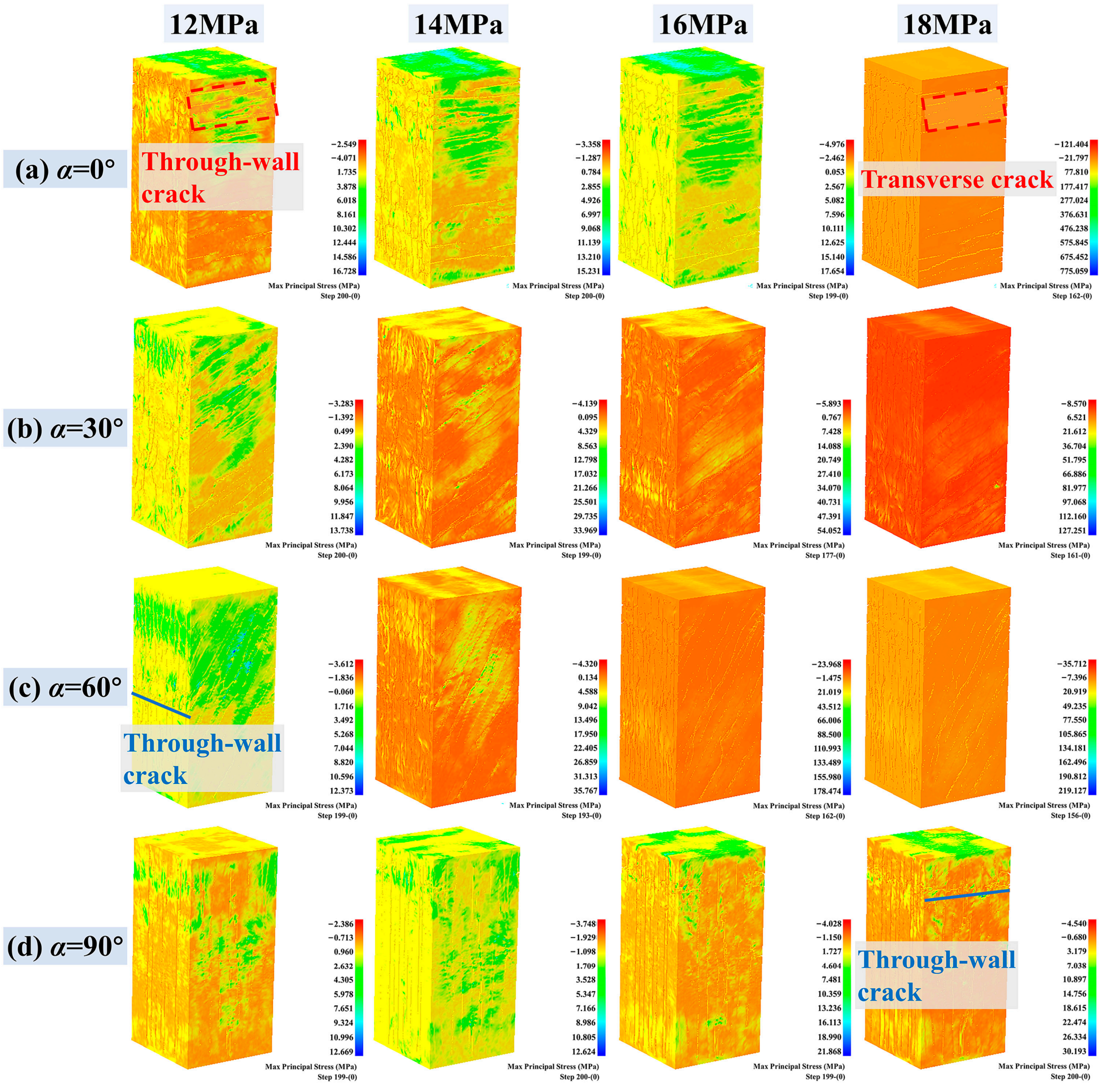

Figure 11. Stress nephogram of the CJRMs under the loading plan II: (**a**) $\alpha = 0°$; (**b**) $\alpha = 30°$; (**c**) $\alpha = 60°$; (**d**) $\alpha = 90°$.

Figure 12 shows the AE events under loading plan II. The AE concentration area is mainly located at the top of the rock mass and parallel to the joint direction. The concentration area in 90° rock mass is distributed transversely to the vertical joints. The increase in peak stress results in more uniform AE energy. At the same time, when the loading rate is constant, the increase in peak stress also promotes the occurrence of compression-shear failure, which is seen clearly in the image of the $\alpha = 30°$ model. When $\alpha = 90°$, the model presents complete tensile failure, and the accumulation area of tensile failure at the top of the rock mass develops from the failure point to the throughline and the penetration surface, as in Figure 11d, which corresponds to the stress nephogram. The AE cloud diagram illustrates that the increase in peak value is conducive to the generation of compression-shear failure and the increase in the proportion of compression-shear failure units. Meanwhile, according to Figure 10b, it can be found that the total number of AE events increases when the peak stress increases and the loading rate is constant.

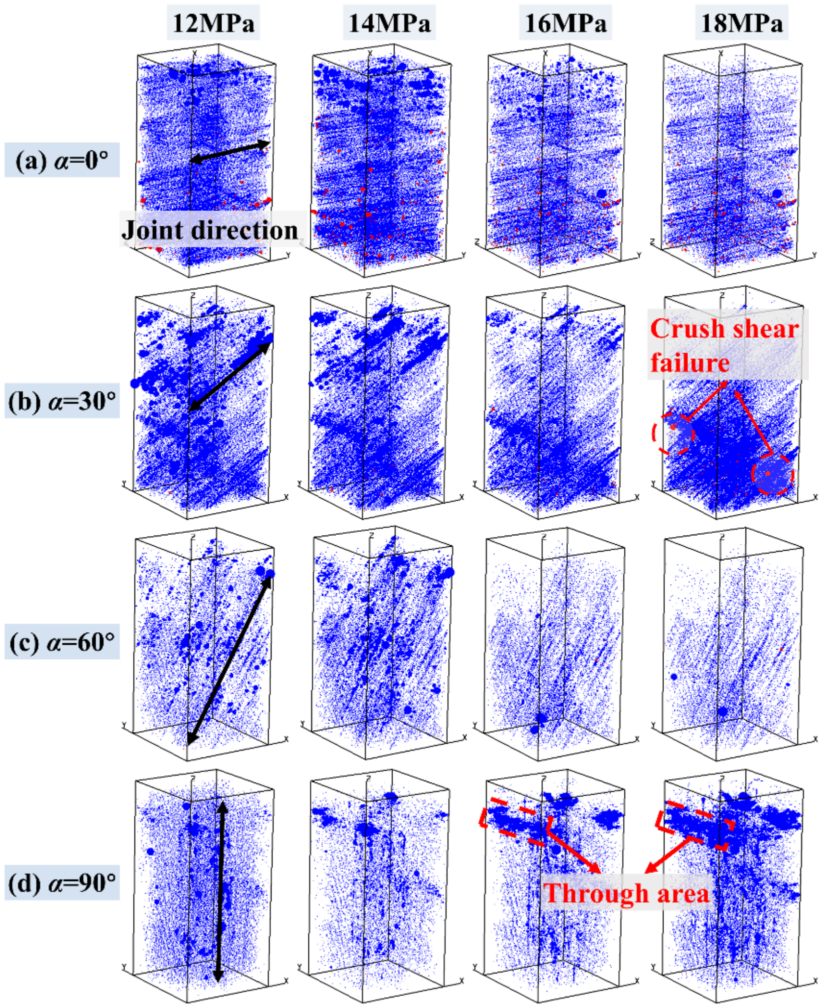

Figure 12. AE diagram of the CJRMs under the loading plan II: (**a**) $\alpha = 0°$; (**b**) $\alpha = 30°$; (**c**) $\alpha = 60°$; (**d**) $\alpha = 90°$.

4.3. Effect of Loading Rate on Failure Mode and AE of Rock Mass

In order to fully consider the effect of the loading rate on the dynamic mechanical properties and failure modes of the CJRMs, four different loading rates are designed, which are 5 μs, 10 μs, 15 μs, and 20 μs to reach the peak strength of 14 MPa. The decay rates are all 10 μs. The numerical simulation analysis of the CJRMs at four angles is carried out.

Figure 13 shows the stress nephogram of the numerical simulation results of CJRM models. The stress distribution of rock mass under dynamic load is not affected by the loading rate. The number of cracks on the surface of rock mass does not change clearly, but the length of cracks increases. At the same time, the crack-free region in the middle of

0° and 30° models do not change. The transverse crack at the top of the 90° models does not form penetrating cracks, as shown in Figure 13d. It can be seen that the change in the loading rate affects the crack length but does not affect the crack distribution. In addition, for the 60° rock mass, the failure time gradually delays as the loading rate slows down. The 30° rock mass appears to be a concentrated area of damage and failure at a high loading rate, as in Figure 13b. Therefore, the loading rate is negatively correlated with the breakout time of rock mass.

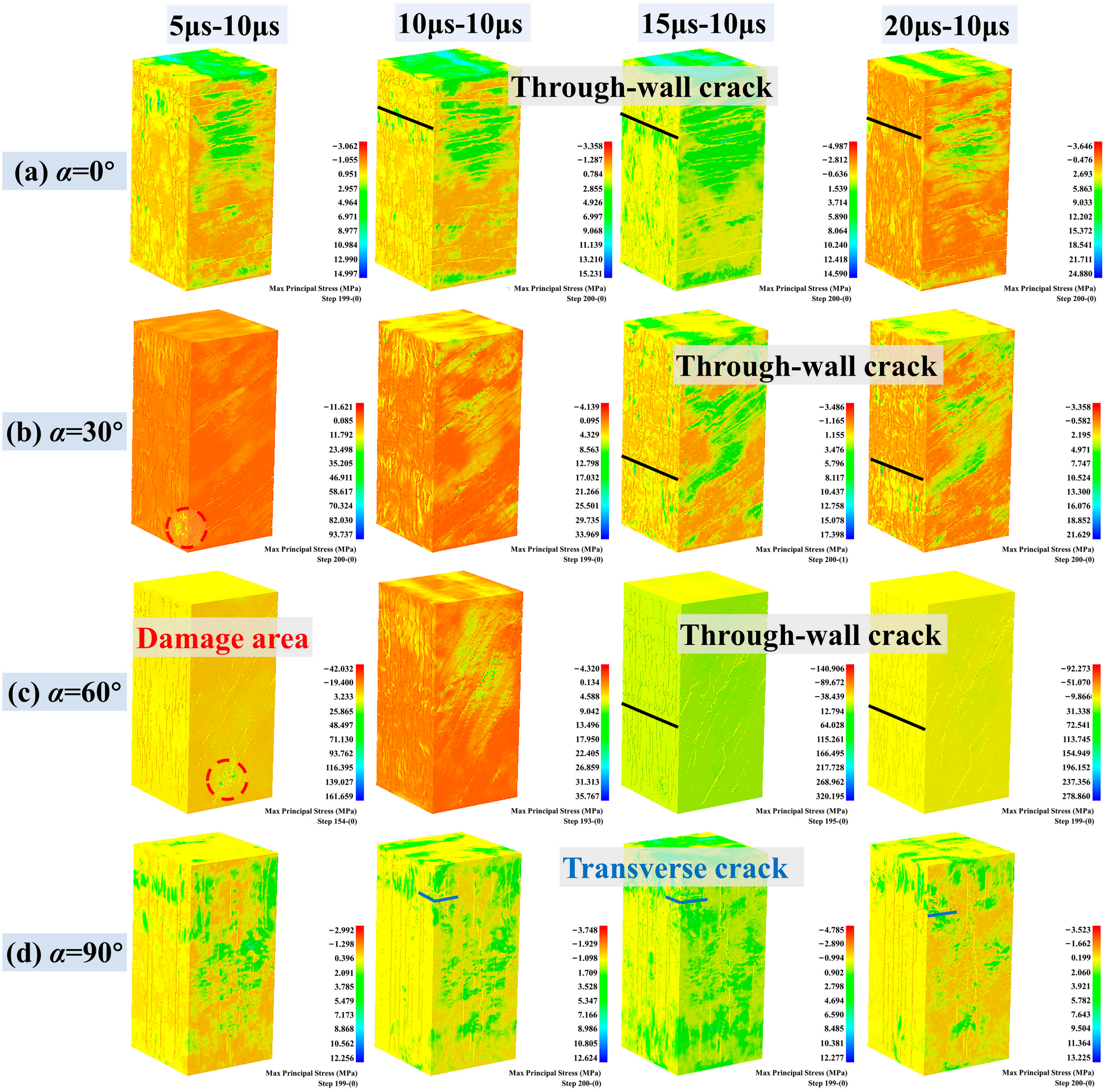

Figure 13. Stress nephogram of the CJRMs under the loading plan III: (**a**) $\alpha = 0°$; (**b**) $\alpha = 30°$; (**c**) $\alpha = 60°$; (**d**) $\alpha = 90°$.

Figure 14 shows the AE cloud image of the CJRM under loading plan III. The aggregation area of tensile AE events appears at the top of the rock mass and is distributed parallel to the joint direction, while the 90° rock mass presents vertical joint direction distribution. The slowing of the loading rate promotes the increase in compression-shear failure range and density (Figure 14a) but does not affect the location of the tensile aggregation area. In addition, a slower loading rate makes the distribution of AE more uniform and increases the total number of AE events. Figure 15 shows the curves of each step AE of the 30° rock mass under loading plan III.

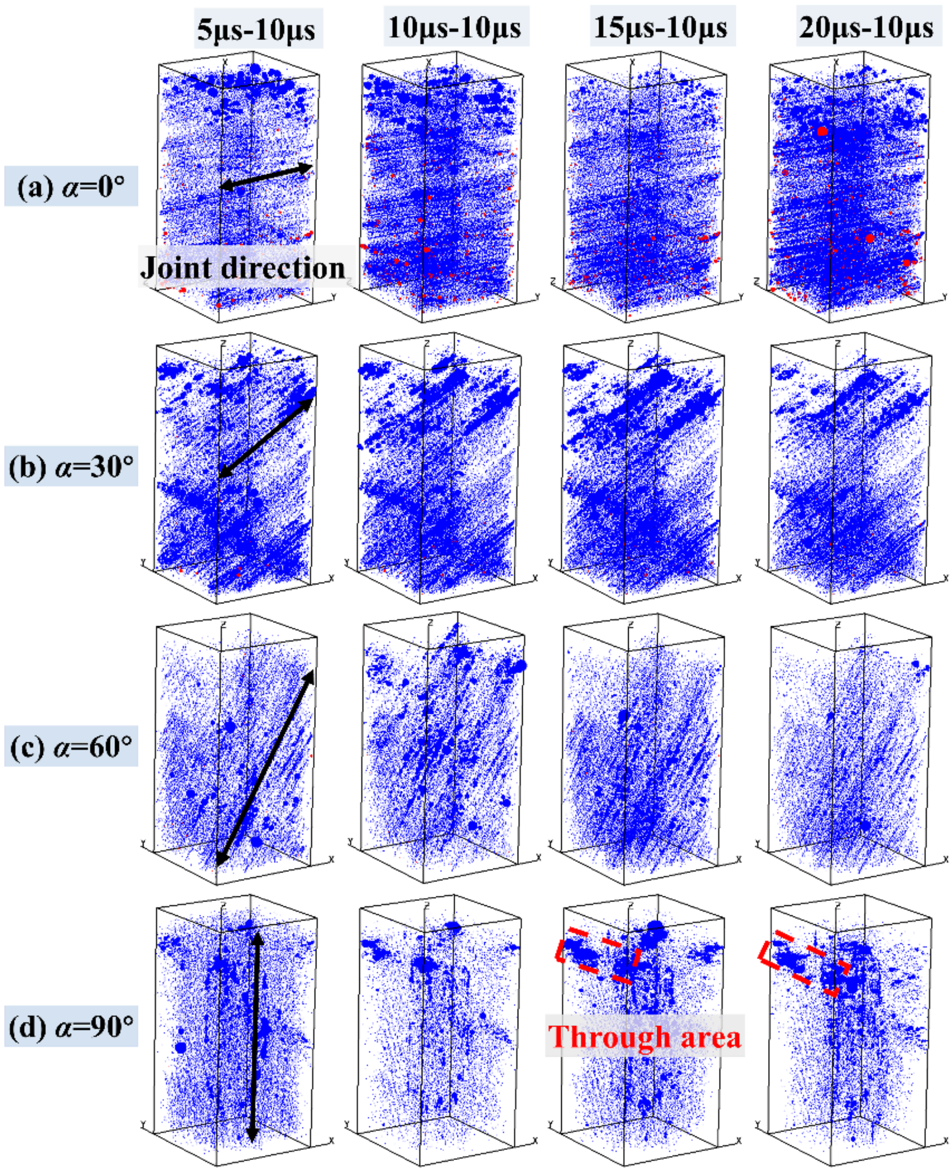

Figure 14. AE diagram of the CJRMs under the loading plan III: (**a**) $\alpha = 0°$; (**b**) $\alpha = 30°$; (**c**) $\alpha = 60°$; (**d**) $\alpha = 90°$.

According to the different responses of rock mass, the dynamic propagation process can be divided into four stages: the accelerated accumulation of AE, the propagation of stress wave to the top, the development of vertical crack to the top, and the rock mass failure stage, as shown in Figure 15a,b. At the same time, it can be observed that with the slow loading rate, the time of different stages is delayed, which explains why there are only three stages in the dynamic propagation process of rock mass in Figure 15c,d. When the loading time is 100 μs, the rock masses do not fail at a low loading rate, so the failure stage is not shown in the curve, which is consistent with the law in Figure 13. Meanwhile, in Figure 15a,b, the time of the accelerated accumulation of AE in the curve is delayed, the energy accumulation speed slows down, the energy accumulation slows down, and the total energy value increases. For the stress propagation stage, the fluctuation of single-step acoustic emission events becomes smaller, and the failure inside the rock mass becomes more uniform. However, when the vertical crack develops to the top of the rock mass, the AE events change dramatically, corresponding to the peak value in the curve. Compared with the four loading rate curves, the peak value of AE events in Figure 15a appears more rapidly and violently at a high loading rate, while the peak value of AE events gradually decreases and increases more gently as the loading rate slows down. On the whole, it can be noted that compared with Figure 15a, the number of single-step AE events in Figure 15d changes more gently, indicating that the rock mass failure is more uniform at a low loading rate, which takes longer time and accumulates more energy.

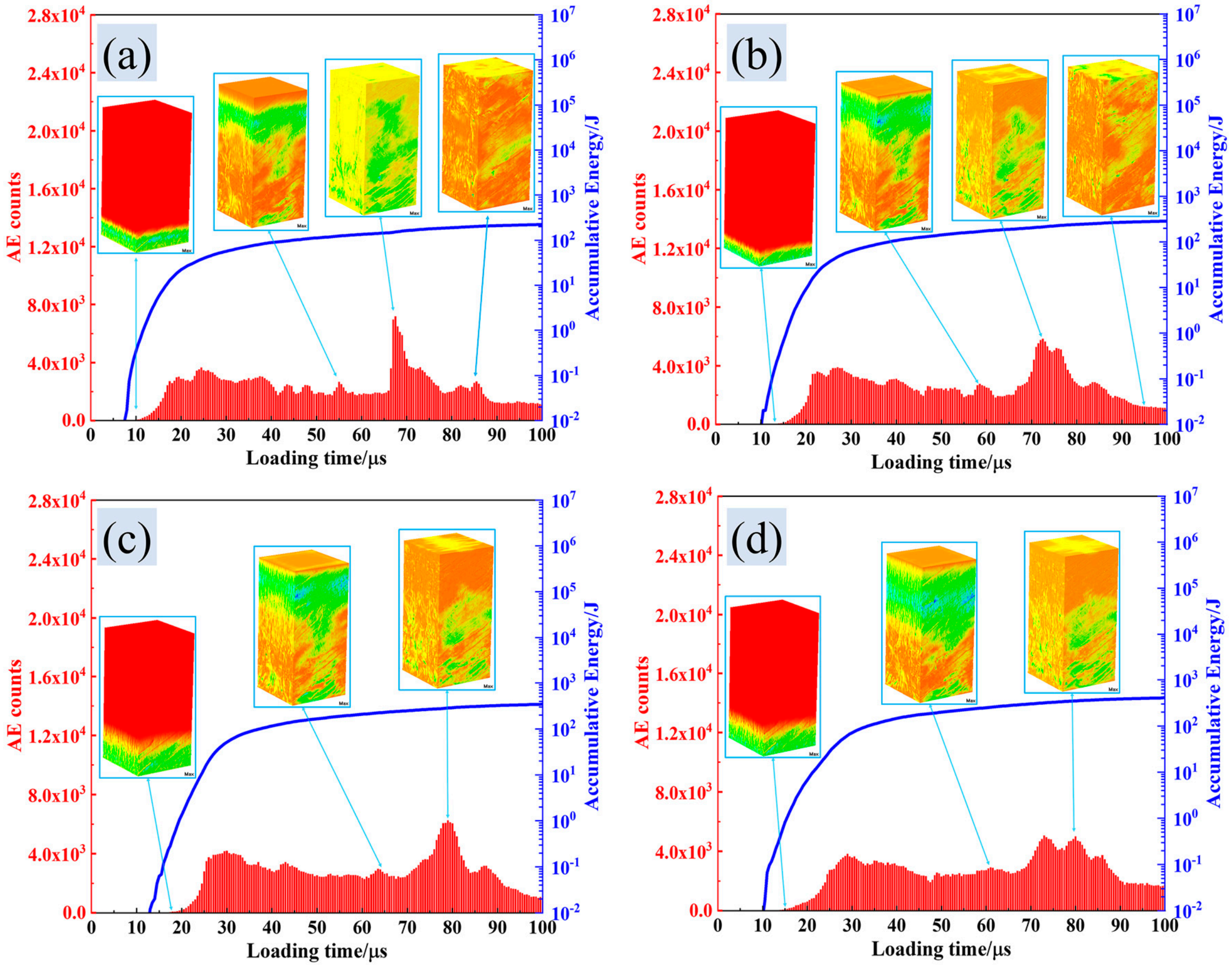

Figure 15. Single step AE and energy curves of loading plan III: (**a**) peak amplitude of 5 μs; (**b**) peak amplitude of 10 μs; (**c**) peak amplitude of 15 μs; (**d**) peak amplitude of 20 μs.

4.4. Effect of Decay Rate on Failure Mode and AE of Rock Mass

Models with four different decay rates were established to study the effect of decay rate on the dynamic mechanical properties and failure mode of the CJRMs. The descending time from the peak strength of 14 MPa to 0 MPa was 5 μs, 10 μs, 15 μs, and 20 μs, respectively, while the loading rate in the models was the same. Numerical simulation analysis was carried out for the CJRMs with four different angles.

Figure 16 shows the stress nephogram results of the CJRM models under loading plan IV. As the decay rate slows down in the 0° models, the stress concentration area inside the rock mass gradually increases, extending from the top to the middle of the rock mass. There is no significant change in the crack geometry and fractured volume of rock mass except for the model with 5 μs in descending time, where the number and development degree of cracks are suppressed, as in Figure 16a. In addition, when the decay rate becomes slower, the failure planes of 30° rock mass and 60° rock mass form earlier. Therefore, the slowing decay rate will increase the maximum stress value and advance the failure time of rock mass. High decay rates inhibit the crack development in rock mass, while low decay rates have little effect on it.

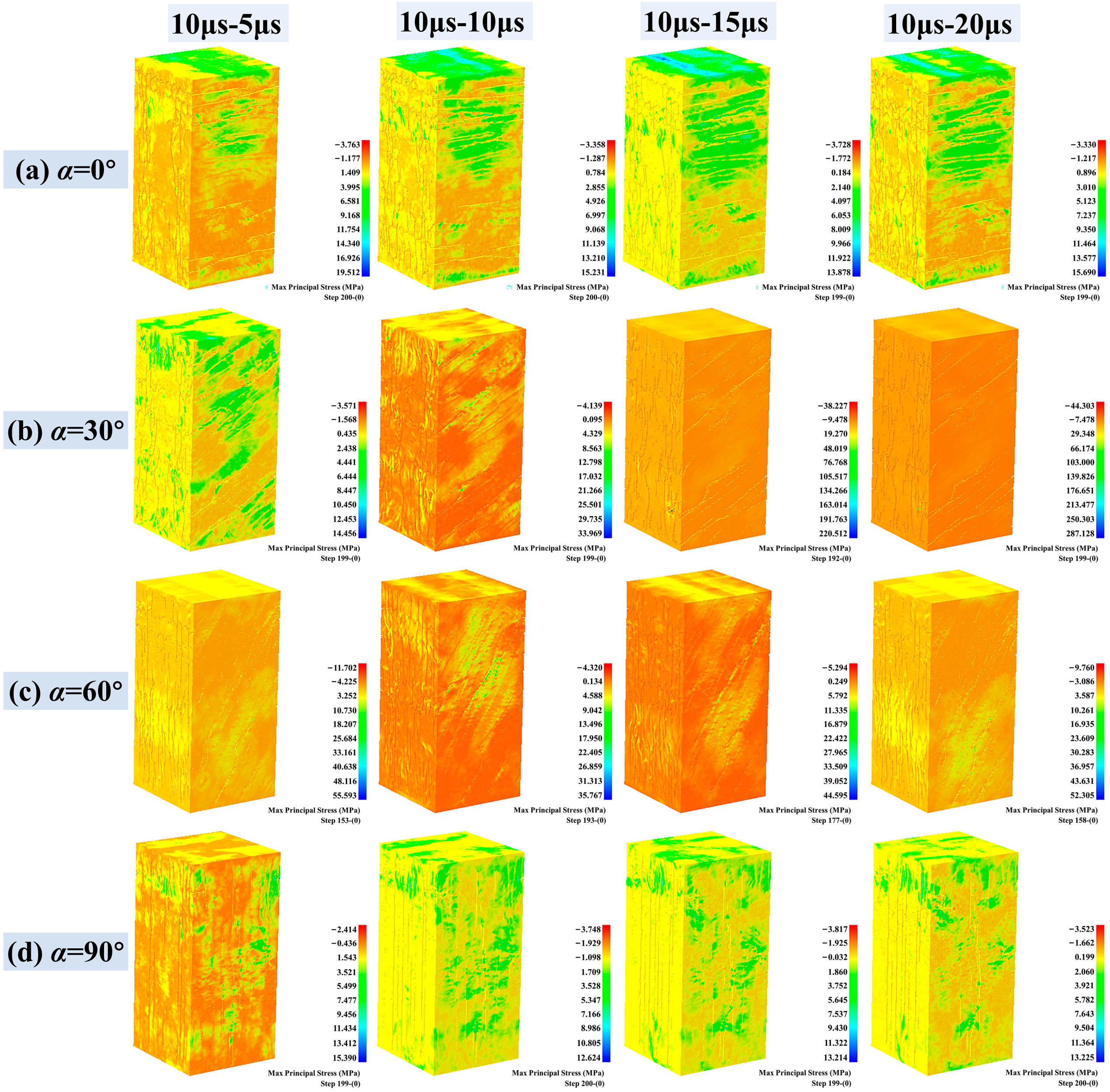

Figure 16. Stress nephogram of the CJRMs under loading plan IV: (**a**) $\alpha = 0°$; (**b**) $\alpha = 30°$; (**c**) $\alpha = 60°$; (**d**) $\alpha = 90°$.

As the decline rate slows down, the number of tensile AE events increases, as in Figure 17. For models with a dip angle of less than 90°, the accessorial events mainly concentrate at the bottom of the models. However, the distribution range of compression-shear failure elements did not change. As for Figure 16b,c, the decay rate slows down, and the rock mass breakout time is advanced so as to form a more tensile failure gathering area and transverse penetration area. Therefore, the slowing decay rate, on one hand, is conducive to reducing the generation of great AE energy; on the other hand, it will increase the compression-shear AE events inside the rock mass and accelerate the fragmentation.

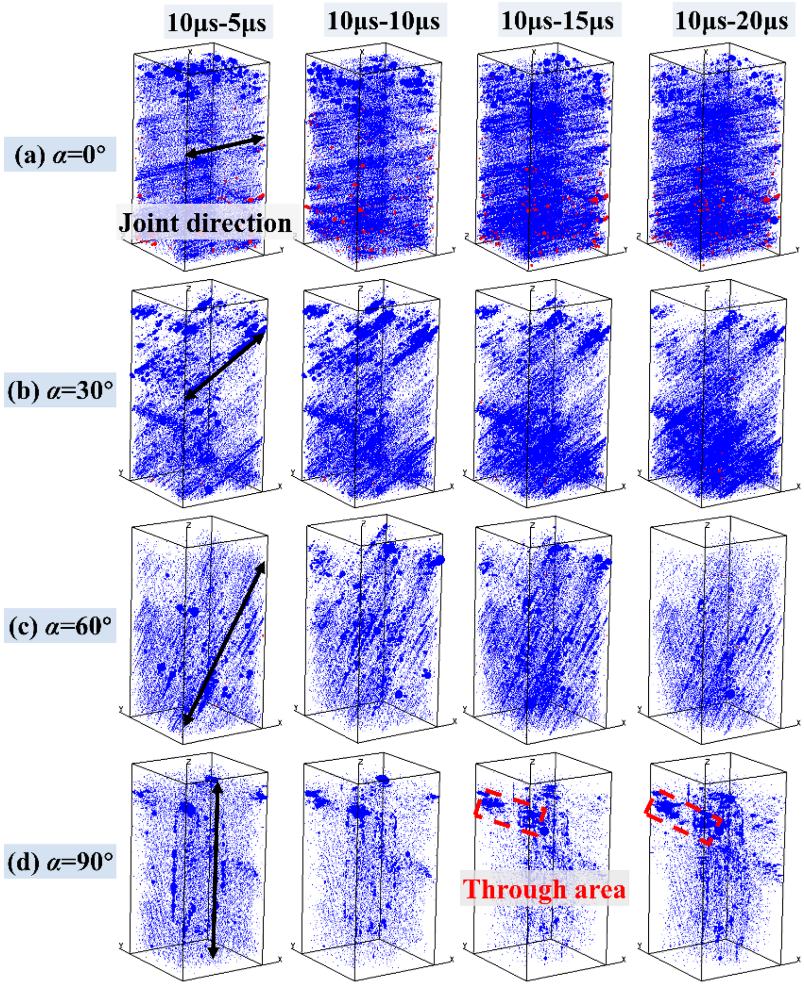

Figure 17. AE diagram of the CJRMs under the loading plan IV: (**a**) $\alpha = 0^\circ$; (**b**) $\alpha = 30^\circ$; (**c**) $\alpha = 60^\circ$; (**d**) $\alpha = 90^\circ$.

5. Discussion

The dynamic failure modes of the CJRMs in this paper are consistent with similar past studies about physical and numerical simulation tests on the dynamic loading of rock mass [42,46,75–77], which concluded that the failure mode of rock mass under dynamic loading is mainly tensile failure and the compressive shear failure of the CJRMs may be determined by the special properties of basalt columns at low angles. Pan et al. [76] studied the dynamic loading of jointed rock mass, and the results show that rock mass with a dip angle of 45-60 is more prone to failure, which is consistent with the thesis in this research that the CJRMs with a dip angle of 60 is the most prone to failure. In addition, cracks in jointed rock mass mainly develop along the joints and are dynamic [77], which is a good mirror of the crack propagation pattern studied in this paper. At the same time, the existence of joints weakens the propagation of stress waves in the rock mass [77], which also explains the reason why there is no crack area in the middle of the CJRMs with low angles.

5.1. Difference of the CJRMs under Dynamic and Static Loading

The failure modes of the CJRMs are different under different loading modes. At present, static load test studies on irregular CJRMs mainly include biaxial compression [58] and true triaxial compression tests with one free face [57]. Under biaxial compression, $\alpha = 30^\circ$ is the most unfavorable dip angle, while under dynamic loading, $\alpha = 60^\circ$ is the most unfavorable dip angle. The main failure modes of CJRMs under biaxial compression are tensile failure along the joint face, mixed tensile-shear failure, shear-slip failure, and disintegration failure of the intercolumnar jointed face. The failure modes of CJRMs under true triaxial compression with one free face are a split failure and shear failure of the columnar jointed structure. However, the failure mode under dynamic loading differs from static. Tensile failure is the primary failure mode, and the number of compression-shear failures decreases with the increase in dip angle. When α = 90°, the model is a complete tensile failure.

In addition, under dynamic loading, the crack development of CJRMs will not stop immediately after the stress disappears but will continue to expand. In contrast, under static loading, the crack stops as soon as the stress or displacement is removed. In dynamic tests, the cracks initiate from the bottom of the rock mass and expand upward, as shown in Figure 18a, and the crack propagation speed along the vertical direction is much greater than that through the joints. The cracks do not develop all the way to the top of the rock mass. When the stress spreads for a period of time, new joints are generated at the top and gradually develop downward. With the propagation of stress, transverse penetrating cracks appear on the side of the rock mass and develop gradually. However, the development of joint cracks does not completely activate all the joint planes, and there is a crack-free area in the middle of the rock mass, which is caused by the different expansion rates of vertical cracks and joint cracks. Moreover, the crack-free region gradually decreases with the increase in the dip angle, as shown in Figure 18b. Under static loading, cracks in rock mass are evenly distributed along the joint direction, and no crack-free zone is observed. At the same time, when a model with $\alpha = 90°$ is under dynamic loading, transverse tensile cracks occur at the top of rock mass, which is also unique for dynamic loading conditions.

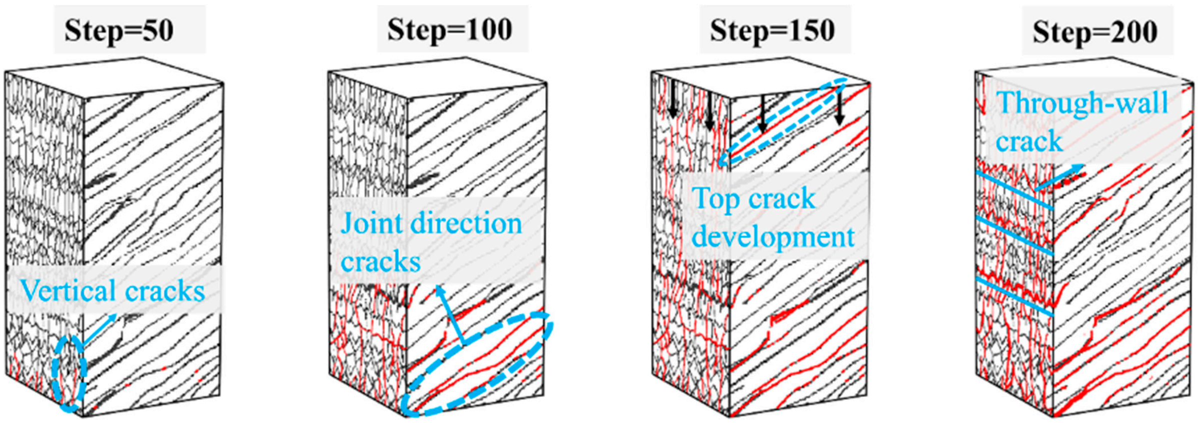

(**a**)

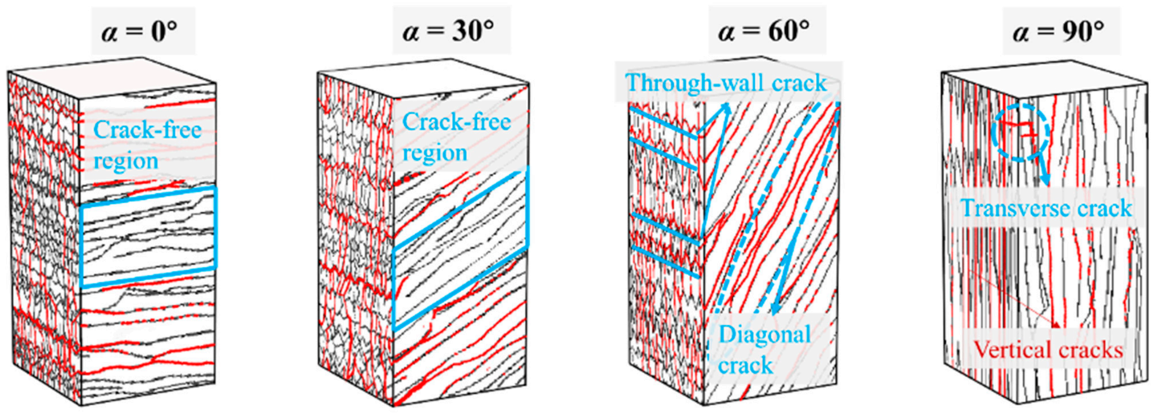

(**b**)

Figure 18. Sketch diagram of cracks of the CJRMs at the peak value of 12 MPa: (**a**) crack development process of $\alpha = 30°$ rock mass; (**b**) cracks in rock mass under different dip angles. Red lines represent the activated joints.

5.2. Differences in the Effects of Loading and Decay Rates

In order to eliminate the influence of loading time on the failure mode of CJRMs, the results of models under different loading rates and decay rates but the same peak amplitude (14 MPa) and wave period are compared.

By comparing Figures 13 and 16, the crack development degree in the slow loading rate model is higher, the stress distribution range is smaller, the fracture time of rock mass is delayed, and the rock mass failure is more dramatic. There are a few differences in the crack development degree caused by the slowing decay rate. The stress distribution range is large, and the time of rock breakout is gradually advanced. In addition, the maximum principal stress of rock mass generated by a high loading rate is larger than that of a high decay rate, while the tensile stress value generated by a low loading rate is smaller than that generated by a low decay rate. A high descending rate can inhibit the crack development of the CJRM. According to the comparison of AE clouds in Figures 14 and 17, a slower loading rate promotes the range and density of compression-shear failures, while the slower decay rate inhibits the range of AE events, but increases the number of compression-shear failures, and speeds up the rock mass fragmentation.

Figure 19 shows the accumulative AE events and energy curves of loading plans III and IV. When the rock mass strength is high, i.e., $\alpha = 0°$ and $90°$, the AE events and energy have an upward trend, and the gradient of loading plan III is greater than that of plan IV. Therefore, the increased AE events and energy caused by the loading rate of rock mass are higher than the decay rate. When the rock mass strength is low, i.e., $\alpha = 30°$ and $60°$, the slowing down rate will promote the rock mass fragmentation and the accumulated AE energy will be larger. Moreover, the influence of loading plan IV is greater than loading plan III, so the AE events and energy of the rock mass caused by the slowing down rate are higher than the loading rate. When $\alpha = 60°$, the AE events and energy curves of rock mass show a "U" shape. In addition, the AE energy of rock mass is higher at a high loading rate and higher at a low decay rate.

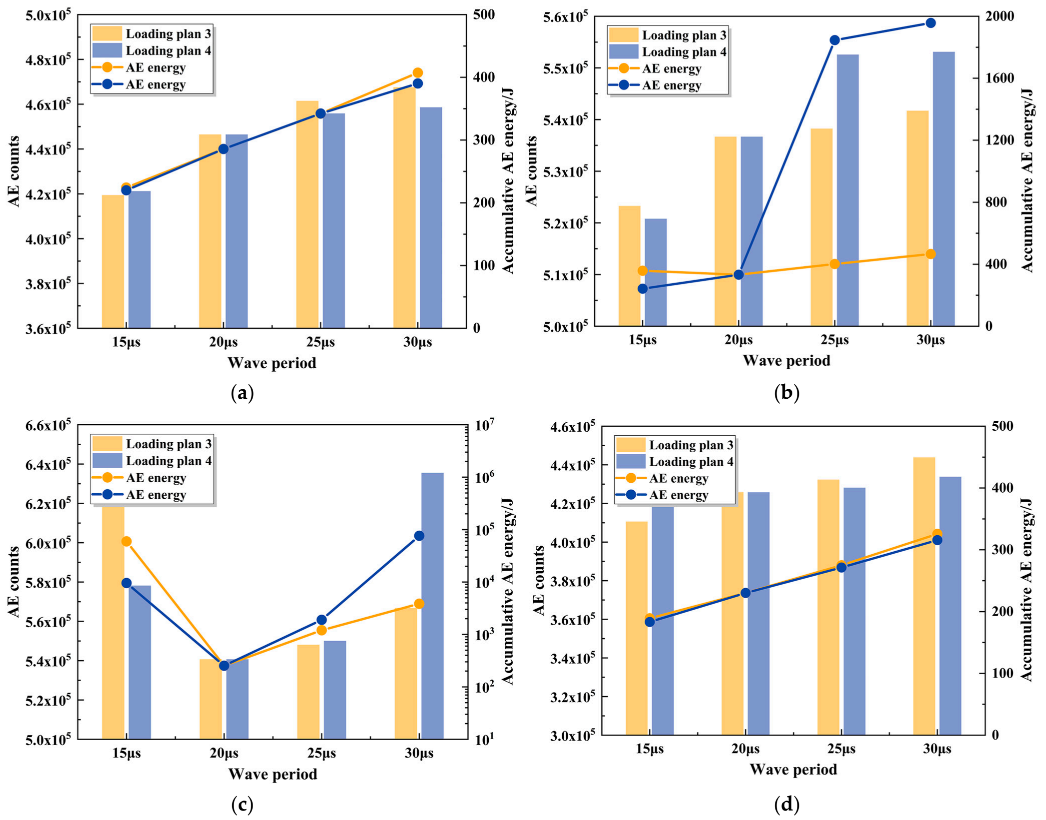

Figure 19. AE events and energy curves of models at the peak value of 14 MPa with different ascending and descending rates and the same loading period: (**a**) $\alpha = 0°$; (**b**) $\alpha = 30°$; (**c**) $\alpha = 60°$; (**d**) $\alpha = 90°$.

5.3. Influence of Dip Angle of CJRM on Failure Mode

The strength of CJRM varies with the change in dip angle. The lowest strength of rock mass is model with 60° in dip angle, followed by 30°, 0°, and the highest is 90°. Therefore, it is important to study the influence of the dip angle of CJRM on dynamic mechanical properties.

With the increase in columnar joint dip angles, the compression-shear failure distribution range and intensity decrease, and the failure mode of rock mass changes from compression-shear-tensile failure (0°) to tensile failure (90°). In addition, the dip angle of CJRM affects the initiation and propagation of cracks. The crack development velocity of rock mass with a dip angle of 0° is less than the propagation velocity of the stress wave, and there is an obvious crack-free area in the middle of the rock mass. With the increase in the dip angle, the region becomes smaller and disappears when it reaches 60°. For the 90° rock mass, the crack develops completely, forming a complete joint-oriented crack network and a penetrating crack perpendicular to the joint-oriented cracks.

The influence of joint dip angle on AE events of rock mass is explored, and AE event curves of four loading plans under different dip angles are drawn in Figure 20. With the increase in the dip angle, the total number of AE events presents an inverted "V" shape, increasing first and then decreasing, which indicates that the CJRMs with 60° joints have more AE events and are more likely to be fractured. Figure 20c shows the different dip curves of loading plans III and IV. It can be noted that the yellow and green curves at 30° and 60° in Figure 20c do not increase significantly, which is because the failure time of the rock mass with the two dip angles is close to each other in the two plans, and no obvious failure area appears. The models are in a steady state, and the intensity of the models with the two angles is close to each other, so the increase in the number of AE events is small. As for the brown curve, the slight decrease is caused by the data error induced by the advance of the rock mass breaking time and the damage evolution mechanism of RFPA for the damage and failed elements. Moreover, for the 60° rock mass, the AE event difference at different loading and decay rates is largest, which further indicates that the 60° rock mass has the lowest strength and is easily affected. In addition, taking the loading time and decay time of 10 µs as the cut-off, when $\alpha = 0°$ and 90°, the influence of a low loading rate is greater than that of a low decay rate, and the influence of a high loading rate is less than that of a high decay rate. When $\alpha = 30°$ and 60°, the influence of a low loading rate is less than that of a low decay rate, and the influence of a high loading rate is more than that of a high decay rate.

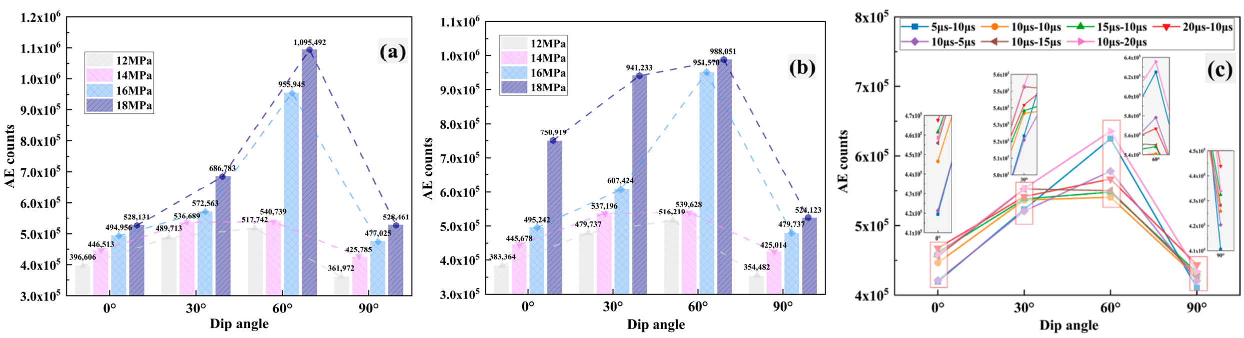

Figure 20. AE event curves of rock mass with changes in different dynamic stress wave parameters at different dip angles: (**a**) Loading plan I; (**b**) Loading plan II; (**c**) Loading plan III and loading plan IV.

6. Conclusions

In this paper, numerical models of irregular CJRMs with different dip angles of the columnar joints (0°, 30°, 60°, and 90°) are established using CT scanning technology and a FEM simulator. By applying four different dynamic loading plans on the bottom of the rock mass, the dynamic failure mode of CJRMs is analyzed, and the influence of stress wave parameters and columnar dip angle on dynamic performance is explored. The conclusions provide references for the engineering construction of underground caverns of rock mass with columnar joints, including the blasting excavation of the caverns, the stability under the earthquake, and the support setting of the caverns. The main conclusions are as follows:

1. In terms of the failure characteristics of the numerical model, the failure modes of different dip angles differ widely. When $\alpha = 0°$, the failure mode is the tension-compression-shear failure parallel to the joint plane, showing a multi-modal of "foreshock—mainshock—aftershock". When $\alpha = 30°$, the tensile failure parallel to the direction of the joint plane is the primary failure mode. A small amount of compression-shear failures is distributed at the bottom and middle of the rock mass, and the failure mode is a multi-model of "foreshock—aftershock". When $\alpha = 60°$, tensile failure takes the dominant position, there are obvious penetrating cracks in the middle of the rock mass, and a few compressive shear failures are distributed at the bottom of the rock mass. The failure mode is the unimodal "aftershock". When $\alpha = 90°$, the rock mass failures are all tensile failures, a transverse tensile crack occurs at the top of the model, and the failure mode is a bimodal "foreshock—aftershock".
2. In terms of the relationship between stress wave parameters and the failure mode, the increase in stress peak value will increase the number of cracks and promote the development of cracks within a certain range. For low-angle rock mass, it will promote the generation of compressive shear failure and increase the ratio of compressive shear failure. The slow loading rate will benefit the crack development but does not affect the crack distribution range. For 0° and 30° rock mass, the distribution range and intensity of compressive shear failure will be increased. The high descending rate inhibits crack development. The slower descending rate increases the compressive shear failure and advances the fracture time but has no obvious effect on crack development. At the same time, when the rock mass strength is high, the AE counts and energy caused by the loading rate are higher than those caused by the decay rate, but the opposite is true when the rock mass strength is low.
3. With the change in dip angle of CJRM, the crack propagation speed in rock mass increases, and the crack-free area decreases with the increase in dip angle. The number of AE events shows an inverted "V" shape, and the rock mass of 60° is the most vulnerable angle, followed by 30°, 0° and 90°. When $\alpha = 0°$ and 90°, the rock mass destruction effect caused by a low loading rate and a high decay rate is greater; and when $\alpha = 30°$ and 60°, the rock mass destruction effect caused by a high loading rate and a low decay rate is greater.

Author Contributions: Conceptualization, Y.X. and C.T.; Formal analysis, B.L. and D.Z.; Funding acquisition, Y.X. and T.L.; Investigation, Y.X. and B.L.; Methodology, Y.X. and C.T.; Project administration, Y.X.; Resources, N.L. and J.C.; Software, T.L. and C.T.; Supervision, C.T.; Validation, B.L., D.Z., and N.L.; Visualization, B.L.; Writing—original draft, Y.X. and B.L.; Writing—review and editing, Y.X. and T.L. All authors have read and agreed to the published version of the manuscript.

Funding: This research was funded by the Open Research Fund of State Key Laboratory of Geomechanics and Geotechnical Engineering, Institute of Rock and Soil Mechanics, Chinese Academy of Sciences (Grant NO. Z020011). The work presented in this paper was also supported by the National Natural Science Foundation of China (Grant Nos. 42077251, 42202305, 41807269, U1865203).

Data Availability Statement: Some or all data that support the findings of this study are available from the corresponding author upon reasonable request.

Conflicts of Interest: The authors declare no conflict of interest.

References

1. Xiao, Y.; Feng, X.; Chen, B.; Feng, G.; Yao, Z.; Hu, L. Excavation-induced microseismicity in the columnar jointed basalt of an underground hydropower station. *Int. J. Rock Mech. Min.* **2017**, *97*, 99–109.
2. Meng, Q.; Wang, H.; Xu, W.; Chen, Y. Numerical homogenization study on the effects of columnar jointed structure on the mechanical properties of rock mass. *Int. J. Rock Mech. Min.* **2019**, *124*, 104127.

3. Hatzor, Y.H.; Feng, X.; Li, S.; Yagoda-Biran, G.; Jiang, Q.; Hu, L. Tunnel reinforcement in columnar jointed basalts: The role of rock mass anisotropy. *Tunn. Undergr. Space Technol.* **2015**, *46*, 1–11.
4. Jin, C.; Yang, C.; Fang, D.; Xu, S. Study on the Failure Mechanism of Basalts with Columnar Joints in the Unloading Process on the Basis of an Experimental Cavity. *Rock Mech. Rock Eng.* **2015**, *48*, 1275–1288.
5. Budkewitsch, P.; Robin, P.Y. Modeling the evolution of columnar joints. *J. Volcanol. Geoth. Res.* **1994**, *59*, 219–239.
6. Jaeger, J.C. The cooling of irregularly shaped igneous bodies. *Am. J. Sci.* **1961**, *259*, 721–734.
7. Weinberger, R.; Burg, A. Reappraising columnar joints in different rock types and settings. *J. Struct. Geol.* **2019**, *125*, 185–194.
8. Goehring, L. Evolving fracture patterns: Columnar joints, mud cracks and polygonal terrain. *Philos. Trans. R. Soc. A* **2013**, *371*, 20120353.
9. Phillips, J.C.; Humphreys, M.C.S.; Daniels, K.A.; Brown, R.J.; Witham, F. The formation of columnar joints produced by cooling in basalt at Staffa, Scotland. *Bull. Volcanol.* **2013**, *75*, 715.
10. Cui, J.; Jiang, Q.; Feng, X.; Li, S.; Liu, J.; Chen, W.; Zhang, J.; Pei, S. Insights into statistical structural characteristics and deformation properties of columnar jointed basalts: Field investigation in the Baihetan Dam base, China. *Bull. Eng. Geol. Environ.* **2018**, *77*, 775–790.
11. Jin, C.; Li, S.; Liu, J. Anisotropic mechanical behaviors of columnar jointed basalt under compression. *Bull. Eng. Geol. Environ.* **2018**, *77*, 317–330.
12. Feng, X.; Hao, X.; Jiang, Q.; Li, S.; Hudson, J.A. Rock Cracking Indices for Improved Tunnel Support Design: A Case Study for Columnar Jointed Rock Masses. *Rock Mech. Rock Eng.* **2016**, *49*, 2115–2130.
13. Fan, Q.; Feng, X.; Weng, W.; Fan, Y.; Jiang, Q. Unloading performances and stabilizing practices for columnar jointed basalt: A case study of Baihetan hydropower station. *J. Rock Mech. Geotech.* **2017**, *9*, 1041–1053.
14. Dai, F.; Li, B.; Xu, N.; Meng, G.; Wu, J.; Fan, Y. Microseismic Monitoring of the Left Bank Slope at the Baihetan Hydropower Station, China. *Rock Mech. Rock Eng.* **2017**, *50*, 225–232.
15. Fan, Q.; Zhou, S.; Yang, N. Optimization design of foundation excavation for Xiluodu super-high arch dam in China. *J. Rock Mech. Geotech.* **2015**, *7*, 120–135.
16. Ji, H.; Zhang, J.C.; Xu, W.Y.; Wang, R.B.; Wang, H.L.; Yan, L.; Lin, Z.N. Experimental Investigation of the Anisotropic Mechanical Properties of a Columnar Jointed Rock Mass: Observations from Laboratory-Based Physical Modelling. *Rock Mech. Rock Eng.* **2017**, *50*, 1919–1931.
17. Smith, J.V.; Holden, L. Rock slope kinematic instability controlled by large-scale variation of basalt column orientation. *Bull. Eng. Geol. Environ.* **2021**, *80*, 239–250.
18. Sonmez, H.; Ercanoglu, M.; Dagdelenler, G. A novel approach to structural anisotropy classification for jointed rock masses using theoretical rock quality designation formulation adjusted to joint spacing. *J. Rock Mech. Geotech.* **2022**, *14*, 329–345.
19. Liu, Z.; Wang, H.; Zhang, C.; Zhou, B.; Zhou, H. Size dependences of the mechanical behaviors of basalt rock blocks with hidden joints analyzed using a hybrid DFN–FDEM model. *Eng. Fract. Mech.* **2021**, *258*, 108078.
20. Mu, W.; Li, L.; Yang, T.; Yu, G.; Han, Y. Numerical investigation on a grouting mechanism with slurry-rock coupling and shear displacement in a single rough fracture. *Bull. Eng. Geol. Environ.* **2019**, *78*, 6159–6177.
21. Jiang, Q.; Feng, X.; Hatzor, Y.H.; Hao, X.; Li, S. Mechanical anisotropy of columnar jointed basalts: An example from the Baihetan hydropower station, China. *Eng. Geol.* **2014**, *175*, 35–45. [CrossRef]
22. Xia, Y.; Zhang, C.; Zhou, H.; Hou, J.; Su, G.; Gao, Y.; Liu, N.; Singh, H.K. Mechanical behavior of structurally reconstructed irregular columnar jointed rock mass using 3D printing. *Eng. Geol.* **2020**, *268*, 105509. [CrossRef]
23. Fan, Q.; Wang, Z.; Xu, J.; Zhou, M.; Jiang, Q.; Li, G. Study on Deformation and Control Measures of Columnar Jointed Basalt for Baihetan Super-High Arch Dam Foundation. *Rock Mech. Rock Eng.* **2018**, *51*, 2569–2595. [CrossRef]
24. Shi, A.; Wei, Y.; Zhang, Y.; Tang, M. Study on the Strength Characteristics of Columnar Jointed Basalt with a True Triaxial Apparatus at the Baihetan Hydropower Station. *Rock Mech. Rock Eng.* **2020**, *53*, 4947–4965. [CrossRef]
25. Zhou, Z.; Wang, P.; Cai, X.; Cao, W. Influence of Water Content on Energy Partition and Release in Rock Failure: Impli-Cations for Water-Weakening on Rock-Burst Proneness. *Rock Mech. Rock Eng.* **2023**, *56*, 6189–6205. [CrossRef]
26. Zhou, Z.; Cai, X.; Li, X.; Cao, W.; Du, X. Response and energy evolution of sandstone under coupled static–dynamic compression: Insights from experimental study into deep rock engineering applications. *Rock Mech. Rock Eng.* **2020**, *53*, 1305–1331. [CrossRef]
27. Wang, Y.; Cao, Z.; Li, P.; Yi, X. On the fracture and energy characteristics of granite containing circular cavity under vari-able frequency-amplitude fatigue loads. *Theor. Appl. Fract. Mec.* **2023**, *125*, 103872. [CrossRef]
28. Wang, Y.; Yan, M.; Song, W. The effect of cyclic stress amplitude on macro-meso failure of rock under triaxial confining pressure unloading. *Fatigue Fract. Eng. M.* **2023**, *46*, 2212–2228. [CrossRef]
29. Jiang, Q.; Feng, X.; Fan, Y.; Zhu, X.; Hu, L.; Li, S.; Hao, X. Survey and Laboratory Study of Anisotropic Properties for Columnar Jointed Basaltic Rock Mass. *Chin. J. Rock Mech. Eng.* **2013**, *32*, 2527–2535.
30. Jiang, Q.; Yang, B.; Yan, F.; Liu, C.; Shi, Y.G.; Li, L.F. New Method for Characterizing the Shear Damage of Natural Rock Joint Based on 3D Engraving and 3D Scanning. *Int. J. Geomech.* **2020**, *20*, 06019022. [CrossRef]
31. Jiang, Q.; Song, L.B.; Yan, F.; Liu, C.; Yang, B.; Xiong, J. Experimental Investigation of Anisotropic Wear Damage for Natural Joints under Direct Shearing Test. *Int. J. Geomech.* **2020**, *20*, 04020015. [CrossRef]
32. Xiao, W.; Deng, R.; Zhong, Z.; Fu, X.; Wang, C. Experimental study on the mechanical properties of simulated columnar jointed rock masses. *J. Geophys. Eng.* **2015**, *12*, 80–89. [CrossRef]

33. Cai, X.; Yuan, J.; Zhou, Z.; Pi, Z.; Tan, L.; Wang, P.; Wang, S.; Wang, S. Effects of hole shape on mechanical behavior and fracturing mechanism of rock: Implications for instability of underground openings. *Tunn. Undergr. Sp. Tech.* **2023**, *141*, 105361. [CrossRef]
34. Deng, X.F.; Chen, S.G.; Zhu, J.B.; Zhou, Y.X.; Zhao, Z.Y.; Zhao, J. UDEC–AUTODYN Hybrid Modeling of a Large-Scale Underground Explosion Test. *Rock Mech. Rock Eng.* **2015**, *48*, 737–747. [CrossRef]
35. Dai, F.; Huang, S.; Xia, K.; Tan, Z. Some Fundamental Issues in Dynamic Compression and Tension Tests of Rocks Using Split Hopkinson Pressure Bar. *Rock Mech. Rock Eng.* **2010**, *43*, 657–666. [CrossRef]
36. Wu, B.; Yao, W.; Xia, K. An Experimental Study of Dynamic Tensile Failure of Rocks Subjected to Hydrostatic Confinement. *Rock Mech. Rock Eng.* **2016**, *49*, 3855–3864. [CrossRef]
37. Fan, L.F.; Wu, Z.J.; Wan, Z.; Gao, J.W. Experimental investigation of thermal effects on dynamic behavior of granite. *Appl. Therm. Eng.* **2017**, *125*, 94–103. [CrossRef]
38. Zhu, J.; Bao, W.; Peng, Q.; Deng, X. Influence of substrate properties and interfacial roughness on static and dynamic tensile behaviour of rock-shotcrete interface from macro and micro views. *Int. J. Rock Mech. Min.* **2020**, *132*, 104350. [CrossRef]
39. Chang, X.; Zhang, X.; Qian, L.Z.; Chen, S.H.; Yu, J. Influence of bedding anisotropy on the dynamic fracture behavior of layered phyllite. *Eng. Fract. Mech.* **2022**, *260*, 108183. [CrossRef]
40. Pei, P.; Dai, F.; Liu, Y.; Wei, M. Dynamic tensile behavior of rocks under static pre-tension using the flattened Brazilian disc method. *Int. J. Rock Mech. Min.* **2020**, *126*, 104208. [CrossRef]
41. Li, D.; Xiao, P.; Han, Z.; Zhu, Q. Mechanical and failure properties of rocks with a cavity under coupled static and dynamic loads. *Eng. Fract. Mech.* **2020**, *225*, 106195. [CrossRef]
42. Gong, F.; Si, X.; Li, X.; Wang, S. Dynamic triaxial compression tests on sandstone at high strain rates and low confining pressures with split Hopkinson pressure bar. *Int. J. Rock Mech. Min.* **2019**, *113*, 211–219. [CrossRef]
43. Yang, W.; Geng, Y.; Zhou, Z.; Li, L.; Gao, C.; Wang, M.; Zhang, D. DEM numerical simulation study on fracture propagation of synchronous fracturing in a double fracture rock mass. *Geomech. Geophys. Geo-Energy Geo-Resour.* **2020**, *6*, 39. [CrossRef]
44. Huang, L. Development and new achievements of rock dynamics in China. *Rock Soil. Mech.* **2011**, *32*, 2889–2900.
45. Huang, J.; Liu, X.; Song, D.; Zhao, J.; Wang, E.; Zhang, J. Laboratory-scale investigation of response characteristics of liquid-filled rock joints with different joint inclinations under dynamic loading. *J. Rock Mech. Geotech.* **2022**, *14*, 396–406. [CrossRef]
46. Wang, F.; Cao, P.; Zhou, C.; Li, C.; Qiu, J.; Liu, Z. Dynamic compression mechanical behavior and damage model of singly-jointed samples. *Geomech. Geophys. Geo-Energy Geo-Resour.* **2020**, *6*, 71. [CrossRef]
47. Li, Y.; Xie, H.; Zhu, Z.; Feng, H.; Ye, J. Study on rules of transmission and reflection of stress wave across fractal joint. *Chin. J. Rock Mech. Eng.* **2009**, *28*, 120–129.
48. Wang, Z.L.; Konietzky, H. Modelling of blast-induced fractures in jointed rock masses. *Eng. Fract. Mech.* **2009**, *76*, 1945–1955. [CrossRef]
49. Zhang, X.; Jiao, Y.; Ma, J. Simulation of rock dynamic failure using discontinuous numerical approach. *Comput. Geotech.* **2018**, *96*, 160–166. [CrossRef]
50. Liao, Z.Y.; Zhu, J.B.; Xia, K.W.; Tang, C.A. Determination of Dynamic Compressive and Tensile Behavior of Rocks from Numerical Tests of Split Hopkinson Pressure and Tension Bars. *Rock Mech. Rock Eng.* **2016**, *49*, 3917–3934. [CrossRef]
51. Islam, M.R.I.; Shaw, A. Numerical modelling of crack initiation, propagation and branching under dynamic loading. *Eng. Fract. Mech.* **2020**, *224*, 106760. [CrossRef]
52. Yilmaz, O.; Unlu, T. Three dimensional numerical rock damage analysis under blasting load. *Tunn. Undergr. Sp. Tech.* **2013**, *38*, 266–278. [CrossRef]
53. Liu, H.Y.; Lv, S.R.; Zhang, L.M.; Yuan, X.P. A dynamic damage constitutive model for a rock mass with persistent joints. *Int. J. Rock Mech. Min.* **2015**, *75*, 132–139. [CrossRef]
54. Ning, L.; Ping, Z.; Duan, Q.W. Dynamic damage model of the rock mass medium with microjoints. *Int. J. Damage Mech.* **2003**, *12*, 163–173. [CrossRef]
55. Li, J.; Ma, G.; Zhao, J. An equivalent viscoelastic model for rock mass with parallel joints. *J. Geophys. Res.* **2010**, *115*, B03305. [CrossRef]
56. Li, J.C.; Ma, G.W. Experimental study of stress wave propagation across a filled rock joint. *Int. J. Rock Mech. Min.* **2009**, *46*, 471–478. [CrossRef]
57. Wang, Q.Z.; Yang, J.R.; Zhang, C.G.; Zhou, Y.; Li, L.; Zhu, Z.M.; Wu, L.Z. Sequential determination of dynamic initiation and propagation toughness of rock using an experimental–numerical–analytical method. *Eng. Fract. Mech.* **2015**, *141*, 78–94. [CrossRef]
58. Li, Y.; Dai, F.; Wei, M.; Du, H. Numerical investigation on dynamic fracture behavior of cracked rocks under mixed mode I/II loading. *Eng. Fract. Mech.* **2020**, *235*, 107176. [CrossRef]
59. Liang, Z.; Qian, X.; Zhang, Y.; Liao, Z. Numerical simulation of dynamic fracture properties of rocks under different static stress conditions. *J. Cent. South Univ.* **2022**, *29*, 624–644. [CrossRef]
60. Qian, X.K.; Liang, Z.Z.; Liao, Z.Y.; Wang, K. Numerical investigation of dynamic fracture in rock specimens containing a pre-existing surface flaw with different dip angles. *Eng. Fract. Mech.* **2020**, *223*, 106675. [CrossRef]
61. Weibull, W. A statistical distribution function of wide applicability. *J. Appl. Mech. T Asme.* **1951**, *18*, 293–297. [CrossRef]

62. Xia, Y.; Liu, B.; Zhang, C.; Liu, N.; Zhou, H.; Chen, J.; Tang, C.A.; Gao, Y.; Zhao, D.; Meng, Q. Investigations of mechanical and failure properties of 3D printed columnar jointed rock mass under true triaxial compression with one free face. *Geomech. Geophys. Geo-Energy Geo-Resour.* **2022**, *8*, 26. [CrossRef]
63. Li, G.; Zhao, Y.; Hu, L.; Qi, S.; Tang, C. Simulation of the rock meso-fracturing process adopting local multiscale high-resolution modeling. *Int. J. Rock Mech. Min.* **2021**, *142*, 104753. [CrossRef]
64. Li, Y.; Jia, H. Numerical simulation and mining width design of extremely inadequate mining of Linnancang coal mine. *Coal. Min. Tech.* **2016**, *21*.
65. Jing, G.; Wang, Y.; Zhou, F.; Tan, Z. Numerical simulation study of water fracturing with different angle through beds holes based on RFPA^{2D}. *Coal. Min. Tech.* **2018**, *23*.
66. Li, T.; Li, L.; Tang, C.; Zhang, Z.; Li, M.; Zhang, L.; Li, A. A coupled hydraulic-mechanical-damage geotechnical model for simulation of fracture propagation in geological media during hydraulic fracturing. *J. Pet. Sci. Eng.* **2019**, *173*, 1390–1416. [CrossRef]
67. Li, T.; Tang, C.; Rutqvist, J.; Hu, M. TOUGH-RFPA: Coupled thermal-hydraulic-mechanical Rock Failure Process Analysis with application to deep geothermal wells. *Int. J. Rock Mech. Min.* **2021**, *142*, 104726. [CrossRef]
68. Xia, Y.; Li, L.; Tang, C.; Li, X.; Ma, S.; Li, M. A new method to evaluate rock mass brittleness based on stress–strain curves of class I. *Rock Mech. Rock Eng.* **2017**, *50*, 1123–1139. [CrossRef]
69. Zhao, D.; Xia, Y.; Zhang, C.; Zhou, H.; Tang, C.A.; Liu, N.; Chen, J.; Wang, P.; Wang, C. Laboratory test and numerical simulations for 3D printed irregular columnar jointed rock masses under biaxial compression. *Bull. Eng. Geol. Environ.* **2022**, *81*, 124. [CrossRef]
70. Zhao, D.; Xia, Y.; Zhang, C.; Tang, C.; Zhou, H.; Liu, N.; Singh, H.K.; Zhao, Z.; Chen, J.; Mu, C. Failure modes and excavation stability of large-scale columnar jointed rock masses containing interlayer shear weakness zones. *Int. J. Rock Mech. Min.* **2022**, *159*, 105222. [CrossRef]
71. Xia, Y.; Zhang, C.; Zhou, H.; Chen, J.; Gao, Y.; Liu, N.; Chen, P. Structural characteristics of columnar jointed basalt in drainage tunnel of Baihetan hydropower station and its influence on the behavior of P-wave anisotropy. *Eng. Geol.* **2020**, *264*, 105304. [CrossRef]
72. Xia, Y.; Zhang, C.; Zhou, H.; Zhang, C.; Hong, W. Mechanical anisotropy and failure characteristics of columnar jointed rock masses (CJRM) in Baihetan Hydropower Station: Structural considerations based on digital image processing technology. *Energies* **2019**, *12*, 3602. [CrossRef]
73. Aydin, A. ISRM Suggested method for determination of the Schmidt hammer rebound hardness: Revised version. *Int. J. Rock Mech. Min.* **2009**, *46*, 627–634. [CrossRef]
74. Li, H.; Li, H.; Gao, B.; Jiang, D.; Feng, J. Study of acoustic emission and mechanical characteristics of coal samples under different loading rates. *Shock Vib.* **2015**, *2015*, 458519. [CrossRef]
75. Luo, Y.; Wang, G.; Li, X.; Liu, T.; Mandal, A.K.; Xu, M.; Xu, K. Analysis of energy dissipation and crack evolution law of sandstone under impact load. *Int. J. Rock Mech. Min.* **2020**, *132*, 104359. [CrossRef]
76. Pan, B.; Wang, X.; Xu, Z.; Guo, L.; Wang, X. Experimental and numerical study of fracture behavior of rock-like material specimens with single pre-set joint under dynamic loading. *Materials* **2021**, *14*, 2690. [CrossRef]
77. Zeng, S.; Jiang, B.; Sun, B. Experimental study on the mechanical properties and crack propagation of jointed rock mass under impact load. *Geotech. Geol. Eng.* **2019**, *6*, 5359–5370. [CrossRef]